Journal of Water Process Engineering 77 (2025) 108421

Contents lists available at ScienceDirect

Journal of Water Process Engineering

journal homepage: www.elsevier.com/locate/jwpe

Magnetic calcium silicate hydrate–oyster shell waste nanocomposite for phosphate removal and recovery: RSM-based optimization, mechanism, and real water application

Chanita Boonkanon [a], Worawit Wongniramaikul [a], Chanadda Phawachalotorn [b], Somsak Limwongsakorn [c], Aree Choodum [a,*]

[a] Integrated Science and Technology Research Center, Faculty of Technology and Environment, Prince of Songkla University, Phuket Campus, Kathu, Phuket 83120, Thailand
[b] King Mongkut's Institute of Technology Ladkrabang, Prince of Chumphon Campus, Chumphon 86160, Thailand
[c] Department of Industrial Technology, Faculty of Science and Technology, Phuket Rajabhat University, Muang, Phuket 83000, Thailand

ARTICLE INFO

Editor: Ludovic F. Dumée

Keywords:
Calcined oyster shell wastes
Calcium silicate hydrate
Iron oxide
Phosphate recovery
Response surface methodology

ABSTRACT

Magnetic nanocomposites offer an effective strategy for phosphate removal from wastewater, preventing eutrophication and enabling phosphate recovery for reuse as fertilizer—supporting a zero-waste approach. In this study, a novel hybrid nanocomposite composed of magnetized calcined oyster shell waste and calcium silicate hydrate (M-COS-CSH) was synthesized through a simple process completed within 5.2 h. Response Surface Methodology was employed for optimization: a Central Composite Design determined the optimal $FeCl_3$ and COS ratios, while a Box–Behnken Design optimized adsorption conditions including adsorbent dose (20–100 mg), initial phosphate concentration (10–90 mg L^{-1}), contact time (15–75 min), and pH (3–11). Under optimal conditions (60 mg adsorbent, 10 mg L^{-1} phosphate, 45 min, pH 6.28), M-COS-CSH achieved a predicted maximum removal efficiency of 97.30 %. An experimental removal efficiency of 98.06 % ± 0.19 % was obtained under the same conditions without pH adjustment (pH 6.84), offering a cost advantage. The adsorption process closely followed the Langmuir isotherm model (R^2 = 0.9963), with a maximum adsorption capacity of 161.29 mg g^{-1}, and was best described by the pseudo-second-order kinetic model (R^2 = 1.0000). Characterization suggested a mechanism involving surface microprecipitation and inner-sphere complexation. Thermodynamic analysis confirmed the process to be endothermic and spontaneous (ΔG°: −9.97 to −10.84 kJ mol^{-1}; ΔH°: 3.00 kJ mol^{-1}; ΔS°: 43.52 J mol^{-1} K^{-1}). M-COS-CSH achieved phosphate removal ranging from 70.81 % ± 2.47 % to 94.24 % ± 0.39 % in real water samples. Even in the presence of competing anions at fivefold phosphate concentration, removal efficiency remained high (93.58 % ± 0.32 %), confirming the material's strong selectivity and suitability in complex matrices.

1. Introduction

Phosphorus (P) is a vital element for life, playing a crucial role in the growth and development of humans, ruminants, and crops [1,2]. Naturally abundant, phosphorus accounts for approximately 0.09 % of the Earth's crust by weight and is predominantly utilized in the production of phosphate fertilizers. However, global phosphorus reserves are increasingly threatened due to the finite availability of phosphate rock resources. This growing scarcity, exacerbated by political and economic challenges, poses serious risks to global food production and security [3,4]. Consequently, phosphorus recovery from phosphorus-contaminated sources, such as wastewater treatment plants (WWTP) effluent has become a critical focus of research and development efforts.

Phosphorus exists in both inorganic forms (such as orthophosphates and condensed phosphates) and organic forms (such as phosphate esters). In natural water systems, orthophosphates typically occur as insoluble phosphate ions (PO_4^{3-}) [5]. However, anthropogenic activities—including agricultural runoff, aquaculture pond effluent, and municipal and industrial discharges—have significantly elevated phosphorus concentrations in aquatic environments [6,7]. Phosphorus levels

* Corresponding author.
E-mail address: aree.c@phuket.psu.ac.th (A. Choodum).

https://doi.org/10.1016/j.jwpe.2025.108421
Received 12 June 2025; Received in revised form 19 July 2025; Accepted 26 July 2025
Available online 6 August 2025

as low as 0.02 mg L^{-1} can trigger eutrophication or algal blooms [7], which severely impact ecosystems, degrade water quality, and threaten public health [8,9]. Recognized for decades as a major global environmental issue [10–12], phosphorus pollution demands immediate and sustained attention. In Thailand, eutrophication driven by plankton blooms remains one of the most pressing water pollution challenges. Total phosphorus (TP) concentrations ranging from 0.25 to 34.80 mg L^{-1} have been reported in urban ponds [13]. Although national regulations have set the phosphorus discharge limit for treated effluent at below 2 mg L^{-1} [14], excessive TP concentrations are still frequently detected in effluents from WWTP that discharge directly into communal drainage waterways [15,16], contributing to nutrient enrichment in coastal ecosystems. Moreover, approximately 36 % of municipal WWTP effluent is reused within communities for activities such as agricultural and green space irrigation, garbage truck washing, road cleaning, and livestock watering [17]. While the reuse of reclaimed water offers significant benefits for water conservation, it may also facilitate the broader dispersion of residual phosphorus into the environment. Therefore, effective phosphorus management strategies are urgently needed to protect environmental quality and public health. In particular, phosphorus should be efficiently removed from water systems and recovered for reuse as fertilizer to support sustainable food production.

Various biological, physicochemical, and hybrid methods have been employed for phosphorus removal. Common techniques include sorption, photocatalysis, chlorination, ozonation, the Fenton reaction, precipitation, ion exchange, enhanced biological phosphorus removal (EBPR) using activated sludge systems, biological trickling filters, biofilm reactors, and fungi-based treatments [18,19]. Although many of these methods can effectively remove phosphorus, they are often not well-suited for its recovery. In contrast, adsorption is particularly favored for both phosphorus removal and recovery due to several advantages, including high efficiency—even at low phosphate concentrations—rapid operation, and cost-effectiveness [20].

A wide range of adsorbents has been explored for phosphorus capture, including nanomaterials, carbon-based materials (such as activated carbon and biochar), chitosan-based materials, calcium-based materials, zirconium-modified materials, polymer-based materials, and various composites [21–26]. Among these, calcium silicate hydrate (CSH) has gained significant attention due to its excellent phosphate adsorption capacity—reported as 65.45 mg g^{-1} [7] and 109.4 mg g^{-1} [27]—which is attributed to its high specific surface area (e.g., 85.22 m^2 g^{-1} [7]; 148.11 m^2 g^{-1} [28]). CSH not only provides abundant surface sites but also releases Ca^{2+} ions, which form complexes with phosphate ions and OH^- ions, which help regulate pH and facilitate calcium phosphate precipitation [29–31]. Moreover, the reaction products, mainly amorphous calcium phosphate (ACP) and hydroxyapatite (HAP), have potential applications as fertilizers [7,27,29,32]. However, a notable limitation of CSH is its intrinsically limited pore structure, which can restrict the release of calcium (Ca^{2+}) and hydroxide (OH^-) ions—both of which are critical for phosphate adsorption and crystallization. Additionally, CSH nanoparticles tend to aggregate in aqueous environments due to their small particle size and high surface free energy [7,27]. This aggregation significantly reduces the effective surface area available for phosphate adsorption, thereby hindering the overall removal efficiency. Furthermore, the fine particle size complicates post-treatment recovery, leading to material loss and increased operational and maintenance costs [7,15,29].

To address these challenges, strategies such as surface modification, magnetization, and compositing CSH with other calcium-based materials have been proposed. Calcium carbonate ($CaCO_3$)-rich waste materials have recently gained significant attention as sustainable, low-cost sorbents for phosphate capture. Various sources have been reported, including cockle shells [33,34], eggshells [35,36], snail shells [37], and chicken bones [38]. Among these, oyster shell waste has demonstrated strong potential for reuse following simple treatment processes, particularly as a fertilizer material [25,39]. Studies have shown that oyster shell waste provides comparable phosphate removal efficiency to reagent-grade $CaCO_3$ [40]. Furthermore, thermal pretreatment can significantly enhance its adsorption capacity [41]. Upon thermal treatment at 800 °C, $CaCO_3$ in oyster shells decomposes into CaO, which offers higher phosphate adsorption capacity due to its greater solubility relative to $CaCO_3$ [25,42,43]. The reuse of oyster shell waste also contributes to food waste reduction and enhances the operational efficiency of waste incineration plants, which often struggle with the high moisture and organic content of food waste. Additionally, magnetizing adsorbents has emerged as an effective approach to facilitate the easy separation and recovery of materials from aqueous systems, aligning with the zero-waste concept. Magnetic materials can bind target compounds and be rapidly separated using an external magnetic field [44–46]. This method reduces the loss of lightweight, non-biodegradable adsorbent particles that could otherwise contribute to secondary water contamination [47,48]. Moreover, magnetite offers the advantages of low toxicity, easy recovery, and favorable adsorption properties [49]. Despite these advances, there remains a lack of integrated materials that combine high reactivity, environmental sustainability, cost-effectiveness, and facile recovery. Furthermore, the application of systematic optimization methods, such as Response Surface Methodology (RSM) to fine-tune both synthesis and adsorption conditions remains underexplored.

To fill this gap, the present study hypothesizes that a magnetized calcium silicate–oyster shell nanocomposite (M-COS-CSH), incorporating a magnetite core, calcined oyster shell (COS), and CSH, can provide enhanced adsorption efficiency, reusability, and environmental compatibility for phosphate removal from wastewater. The hypothesis is grounded in the synergistic effects of the component materials: COS offers high calcium content for phosphate precipitation, CSH provides a reactive and high-surface-area matrix, and magnetite enables recovery and reuse. This study presents a novel, low-cost, and sustainable nanocomposite, synthesized via a facile and time-efficient method, and systematically optimized using RSM. The developed material was comprehensively characterized, and its adsorption behavior was investigated through isotherm, kinetic, and thermodynamic analyses to elucidate the underlying mechanisms. In addition, the effects of coexisting anions commonly found in natural and wastewater matrices were assessed to evaluate selectivity. The reusability of the nanocomposite was also tested to determine its stability and performance over multiple adsorption–desorption cycles. Finally, the practical applicability of M-COS-CSH was demonstrated using real water samples, highlighting its strong potential for sustainable phosphate management in real-world environmental applications. This work offers a significant advancement in the development of multifunctional sorbents for sustainable phosphorus management, bridging material innovation and environmental application.

2. Materials and methods

All materials used in this study are listed in Supplementary Material S1.

2.1. Preparation of M-COS-CSH

COS was prepared following the method of [25]. Cleaned oyster shell waste was crushed and sieved to obtain particles ≤0.125 mm, then calcined at 900 °C for 3 h. The resulting light grey powder was stored in a desiccator for future use.

M-COS-CSH was synthesized using a modified procedure based on established methods [7,25,46]. In a 250 mL round-bottom flask, optimized amounts of $FeCl_3$ and $FeSO_4$ (as determined by RSM) were dissolved in 20 mL of ultrapure water and stirred magnetically. The mixture was then heated in a water bath at 80 °C for 30 min. Subsequently, a 0.84 % (*w/v*) NaOH solution was added dropwise, immediately turning the solution black—indicative of magnetite (Fe_3O_4) formation. After cooling to room temperature, COS and Na_2O_3Si (13.78 g) were added,

and the mixture was stirred for 1 h. This was followed by 10 min of sonication, during which a 47 % (*w/v*) $CaCl_2$ solution was gradually added dropwise, resulting in the immediate formation of a black sol–gel. The resulting product was then soaked in 4 L of ultrapure water for 30 min to remove unreacted $Ca(OH)_2$, filtered through a 0.45 μm membrane, and oven-dried at 80 °C. The final composite was stored in a desiccator until use. Detailed procedures for the preparation of Fe_3O_4, CSH, and COS-CSH nanocomposites used for comparison are provided in Supplementary Materials S2 to S4. A schematic illustration of the M-COS-CSH synthesis is presented in Supplementary Fig. S1.

2.2. Experimental design

RSM was employed to optimize both the synthesis conditions of M-COS-CSH and the parameters for phosphate adsorption. A Central Composite Design (CCD) was used to optimize the preparation of M-COS-CSH, while a Box-Behnken Design (BBD) was applied for optimizing phosphate adsorption conditions. The actual and coded values of the independent variables are summarized in Table 1. For the CCD, two independent variables were evaluated at five levels, coded as −α, −1, 0, + 1, and + α, with α calculated as $(2^k)^{1/4} = 1.414$, where *k* is the number of variables. In the BBD, four independent variables were tested at three levels (−1, 0, and + 1). The number of experimental trials was determined using the formulas $2^k + 2k + C$ for CCD [50], and 2 k(k − 1) + C for BBD [51], where *C* represents the number of central points. In both designs, the response variable (*Y*) was phosphate removal efficiency (RE, %), with values approaching 100 % considered optimal. The actual weights of the ingredients used for M-COS-CSH preparation are provided in Supplementary Table S1, and the coded experimental design for CCD optimization is presented in Supplementary Table S2. Experimental design generation and statistical analyses, including regression modeling, response surface plotting, and analysis of variance (ANOVA), were performed using STAT-EASE 360 software (USA).

2.3. Characterization of M-COS-CSH

The M-COS-CSH nanocomposite, both before and after phosphate adsorption, was characterized using a range of instrumental techniques. A high-throughput surface area and porosity analyzer (ASAP 2460, Micromeritics, USA) was used to determine the specific surface area, porosity, and pore size distribution of the samples. Nitrogen adsorption–desorption isotherms were measured, and the data were analyzed using the Brunauer–Emmett–Teller (BET) method for surface area and the Barrett–Joyner–Halenda (BJH) method for pore size distribution.

Table 1
Variables with actual and code values for response surface experiment and the values of phosphate adsorption.

Independent variables	Symbol	Level					C	Run order
		−α (−1.414)	Low (−1)	Central (0)	High (−1)	+α (+1.414)		
i) CCD: Preparation of M-COS-CSH								
$FeCl_3$ (g)	A	2.98	4.32	7.56	10.80	12.14	1	9
COS (g)	B	0.53	0.90	1.80	2.70	3.07		
ii) BBD: Adsorption of phosphate								
Dose of adsorbent (mg)	A	–	20	60	100	–	3	27
Initial concentration (mg L^{-1})	B	–	10	50	90	–		
Contact time (min)	C	–	15	45	75	–		
pH	D	–	3	7	11	–		
Response: Removal efficiency (%)	Y							

Run order	Actual variables				Code variables				Actual (%RE)	Predicted (%RE)
BBD	A: Dose (mg)	B: Initial Concentration (mg L^{-1})	C: Contact time (min)	D: pH	A	B	C	D		
1	20	10	45	7	−1	−1	0	0	68.98	61.84
2	100	10	45	7	1	−1	0	0	92.60	91.64
3	20	90	45	7	−1	1	0	0	21.58	24.02
4	100	90	45	7	1	1	0	0	83.43	92.06
5	60	50	15	3	0	0	−1	−1	89.17	93.15
6	60	50	75	3	0	0	1	−1	95.68	90.57
7	60	50	15	11	0	0	−1	1	56.30	62.90
8	60	50	75	11	0	0	1	1	90.53	88.04
9	20	50	45	3	−1	0	0	−1	52.30	56.58
10	100	50	45	3	1	0	0	−1	93.66	92.37
11	20	50	45	11	−1	0	0	1	23.30	27.06
12	100	50	45	11	1	0	0	1	90.92	89.11
13	60	10	15	7	0	−1	−1	0	90.60	93.66
14	60	90	15	7	0	1	−1	0	67.44	64.61
15	60	10	75	7	0	−1	1	0	89.30	94.60
16	60	90	75	7	0	1	1	0	86.84	86.24
17	20	50	15	7	−1	0	−1	0	43.63	38.53
18	100	50	15	7	1	0	−1	0	94.87	89.16
19	20	50	75	7	−1	0	1	0	49.77	51.53
20	100	50	75	7	1	0	1	0	97.58	98.73
21	60	10	45	3	0	−1	0	−1	92.94	93.86
22	60	90	45	3	0	1	0	−1	88.44	85.67
23	60	10	45	11	0	−1	0	1	89.17	87.99
24	60	90	45	11	0	1	0	1	63.64	58.77
25	60	50	45	7	0	0	0	0	94.38	92.56
26	60	50	45	7	0	0	0	0	92.49	92.56
27	60	50	45	7	0	0	0	0	90.82	92.56

Prior to analysis, the samples were degassed at 200 °C for 6 h. Nitrogen gas was used as the adsorbate at 77.35 K. Surface morphology was examined using field emission scanning electron microscopy (FE-SEM; FEI, Eindhoven, Netherlands), with samples sputter-coated with gold to minimize charging and enhance image clarity. Elemental composition was determined using energy-dispersive X-ray spectroscopy (EDX) integrated with the FE-SEM system. Functional groups on the adsorbents were identified using Fourier-transform infrared (FTIR) spectroscopy (Nicolet iS50 FT-IR; Thermo Fisher Scientific, WI, USA), with spectra recorded in the range of 4000–400 cm^{-1} using the KBr pellet method. Crystalline phases and structural composition were characterized by X-ray diffraction (XRD; PANalytical Empyrean, Eindhoven, Netherlands) using CuKα radiation (λ = 0.154 nm), scanned over a 2θ range of 5–90°. X-ray photoelectron spectroscopy (XPS; ULVAC-PHI, MN, USA) was performed to investigate the surface chemical states and elemental composition. Magnetic properties were measured using a vibrating sample magnetometer (VSM; Lake Shore Cryotronics, OH, USA) under a maximum applied magnetic field of 10,000 Oe, with data collected at over 160 points. Additional characterization details are provided in Supplementary Material S5.

2.4. Phosphate adsorption experiments and application to real water samples

Phosphate adsorption experiments were conducted using a batch system, with detailed procedures provided in Supplementary Material S6. The adsorption mechanism, isotherm behavior, kinetics, and thermodynamic properties were systematically investigated, as described in Supplementary Material S7. Real water samples were collected in February 2025 from municipal wastewater, effluent, and reverse osmosis (RO) concentrate streams in Patong, Phuket, Thailand. Additional samples were randomly collected from three coastal seawater locations near the Vichit, Chalong, and Patong piers. Each 100 mL water sample was treated with 0.06 g of M-COS-CSH under magnetic stirring for 45 min at room temperature, without pH adjustment. Phosphate removal efficiency and adsorption capacity were then determined. In addition, chemical oxygen demand (COD) and total suspended solids (TSS) were measured before and after the adsorption process, with measurement procedures detailed in Supplementary Material S8. The effects of coexisting ions on phosphate removal efficiency and the reusability of M-COS-CSH were also evaluated, following procedures adapted from previous studies [15,52].

3. Results and discussion

3.1. Optimization of M-COS-CSH preparation

The experimental design for the synthesis of M-COS-CSH was performed using a CCD, with two independent variables: A (amount of $FeCl_3$) and B (amount of COS), while the amount of $FeSO_4$ was kept at a constant ratio relative to $FeCl_3$. The other components used for CSH preparation were also held constant. A total of nine experimental runs were conducted based on the coded levels of the variables, resulting in removal efficiencies (RE) ranging from 78.63 % to 88.44 % (Supplementary Table S2). The data were fitted to a two-factor interaction (2FI) model, resulting in the final model expressed in Eq. (1), where a positive coefficient indicates a synergistic effect and a negative coefficient indicates an antagonistic effect. The predicted RE values ranged from 78.31 % to 88.50 %. The ANOVA showed a model *p*-value of 0.0065 and an F-value of 14.66, indicating that the model is statistically significant (Supplementary Table S3). The model exhibited a high coefficient of determination (R^2 = 0.8979), indicating that approximately 89.8 % of the variability in the response was explained by the fitted model, thus demonstrating strong agreement with the experimental data. The adjusted R^2 of 0.8367 accounts for the number of predictors in the model and confirmed the model's robustness by penalizing the inclusion of non-significant terms. Meanwhile, the predicted R^2 of 0.7587 evaluates the model's ability to predict new observations. The relatively small difference (less than 0.2) between the adjusted and predicted R^2 values indicated good model consistency and strong predictive performance [53,54].

$$\text{Removal efficiency}\ (\%) = 82.27 - 2.15\,A + 2.80B - 1.28AB \quad (1)$$

The effects of synthesis variables at their central coded levels (coded value = 0) are illustrated in the perturbation plot (Supplementary Fig. S2) and profiler plot (Supplementary Fig. S3). The profiler plot showed that increasing $FeCl_3$ (variable A) markedly reduced phosphate removal efficiency (Supplementary Fig. S3a), indicating that a lower $FeCl_3$ amount—serving as the magnetite precursor—enhances adsorption performance. This trend aligns with preliminary results, where RE dropped from 97.46 % ± 0.78 % to 95.18 % ± 1.74 % as $FeCl_3$ increased from 4.32 to 10.8 g. The decline is likely attributed to the reduced proportion of active components (CSH and COS) when more $FeCl_3$ is added, given the fixed total adsorbent mass. Notably, phosphate quantification in preliminary tests used membrane filtration rather than magnetic separation. When magnetic separation was applied, lower $FeCl_3$ content weakened the magnetic response due to reduced magnetite, leading to adsorbent loss and reduced durability. Recovery improved significantly with higher $FeCl_3$, increasing from 44.86 % ± 1.46 % to 87.67 % ± 2.16 % (Supplementary Fig. S3c). The reduced RE at low $FeCl_3$ levels under magnetic separation was likely due to incomplete removal of suspended phosphate-loaded adsorbent, resulting in underestimated phosphate removal. These findings underscore the need for sufficient magnetization to prevent adsorbent loss and ensure efficient removal. However, excessive magnetite raises concerns about Fe leaching. ICP-OES analysis showed Fe^{2+} concentrations rose from 0.075 ± 0.002 to 0.141 ± 0.053 mg L^{-1} as $FeCl_3$ dosage increased from 4.32 to 10.8 g. Therefore, 7.56 g of $FeCl_3$ offers an optimal balance between magnetic recovery, phosphate removal efficiency, and minimal Fe leaching.

Regarding COS (variable B), the perturbation plot indicated a strong positive effect on phosphate removal. Both RE and adsorption capacity increased with higher COS amounts (Supplementary Fig. S3b), consistent with preliminary data (Supplementary Fig. S3d). Compared to $FeCl_3$, COS exerted a more pronounced effect, as reflected in the steeper perturbation slope. Based on these findings, the optimal synthesis conditions were 7.56 g of $FeCl_3$ and 2.70 g of COS. The resulting M-COS-CSH (50 mg) achieved a phosphate RE of 95.52 % ± 0.57 % phosphate removal from a 20 mg L^{-1} solution in 30 min. Contour and three-dimensional response surface plots illustrating the effects of $FeCl_3$ and COS amounts during the synthesis of M-COS-CSH on phosphorus adsorption are presented in Fig. 1a.

In addition, a comparative analysis was conducted among M-COS-CSH and other active materials, including COS, CSH, COS-CSH, and magnetite (Fe_3O_4), as summarized in Supplementary Table S4. The incorporation of COS and CSH, combined with magnetization, not only enhanced the recovery of fine particles via magnetic separation but also moderated the final pH of the treated solution, thereby reducing the need for additional neutralization prior to discharge. Among the non-composite materials, CSH exhibited the lowest phosphate RE (83.34 % ± 2.94 %), likely due to its relatively large particle size, which led to a reduced surface area. COS alone achieved higher efficiency (98.02 % ± 0.44 %) but released a greater amount of hydroxide ions, resulting in an elevated final pH and potentially increased neutralization costs. The COS-CSH composite (without magnetization) improved both RE (97.94 % ± 0.27 %) and pH control; however, the recovery of fine particles remained challenging. In contrast, M-COS-CSH maintained a high phosphate RE (97.23 % ± 0.55 %) while enabling facile magnetic separation and achieving a more balanced final pH—contributing to overall cost-effectiveness. Both COS and CSH were confirmed as active components for phosphate adsorption, whereas Fe_3O_4 alone demonstrated negligible performance, with a RE of only 3.93 % ± 0.41 %.

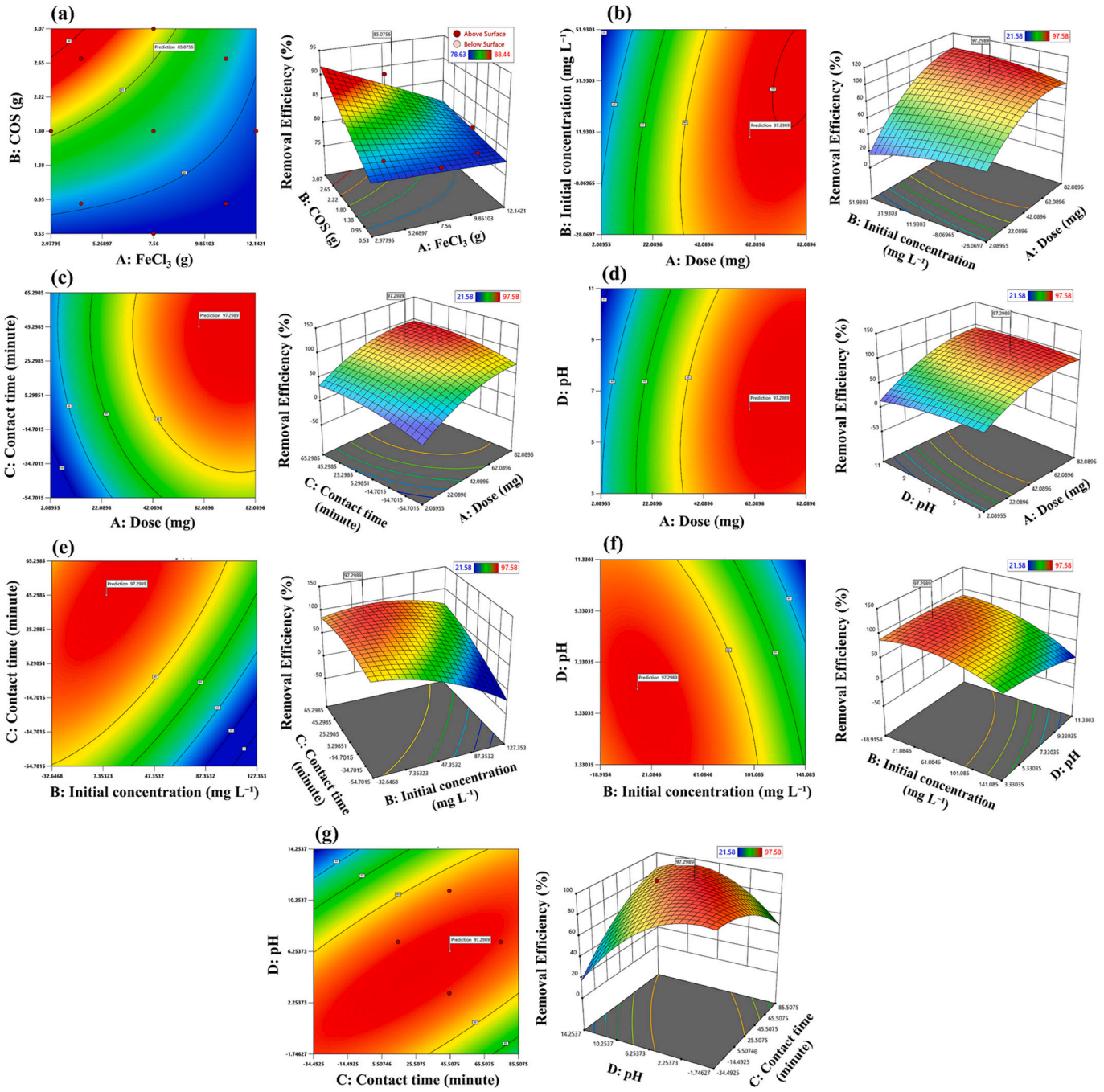

Fig. 1. Contour and three-dimensional response surface plots illustrating the effects of various parameters on phosphorus adsorption: (a) $FeCl_3$ and COS amounts during the synthesis of M-COS-CSH; (b) M-COS-CSH dose and initial phosphate concentration; (c) M-COS-CSH dose and contact time; (d) M-COS-CSH dose and solution pH; (e) initial phosphate concentration and contact time; (f) initial phosphate concentration and solution pH; (g) contact time and solution pH.

3.2. *Characterization of M-COS-CSH*

The M-COS-CSH nanocomposites synthesized in this study appeared as fine, dark grey particles (Fig. 2a and Supplementary Fig. S4). While CSH and COS typically exhibit white to creamy coloration, the incorporation of Fe_3O_4 for magnetization imparted a dark grey hue to the nanocomposite. The average particle size was 781.2 ± 12.3 nm, with a zeta potential of −10.87 ± 0.52 mV at pH 10.67.

FE-SEM imaging of M-COS-CSH nanocomposites revealed a porous architecture with interconnected microchannels, formed by agglomerated spherical and irregularly shaped clusters (Fig. 2b). This morphology resembles that reported for calcined oyster shell waste [25], calcined eggshells [36,55], and calcium oxide nanoparticles [56]. At higher magnification (Fig. 2c), a honeycomb-like structure—characteristic of CSH—was clearly observed, consistent with previous studies [27,57]. In addition, the M-COS-CSH structure featured warped nanosheets intersecting to form a relatively uniform nanoporous network. This warping likely resulted from the loss of some bridging silicates during synthesis, leading to the displacement, tilting, and rotation of silicate chains [7,27,58]. Such a structure provides a favorable surface for phosphate adsorption due to its high surface area and interconnected porosity. Morphological analysis suggests that COS domains are integrated within the CSH matrix, while magnetite particles form a core–shell configuration in the nanocomposite. This is consistent with previous transmission

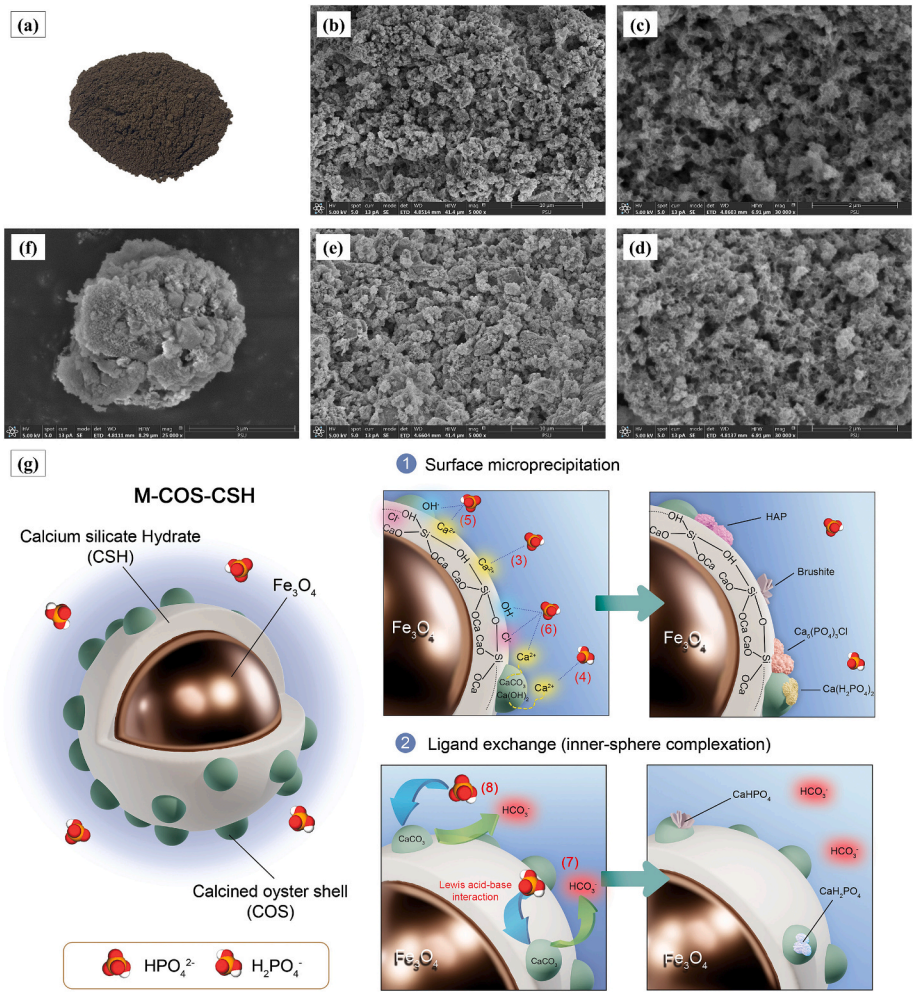

Fig. 2. (a) Photograph of the M-COS-CSH nanocomposite; (b–c) FE-SEM images of M-COS-CSH before phosphate adsorption at magnifications of 5000× and 25,000×, respectively; (d–f) FE-SEM images after phosphate adsorption at 5000×, 25,000×, and 30,000×, respectively; and (g) Schematic illustration of the proposed adsorption mechanism of M-COS-CSH, involving surface microprecipitation and ligand exchange.

electron microscopy (TEM) observations, which showed Fe_3O_4 nanoparticles embedded as dark cores within a lighter CSH matrix composed of warped thin nanosheets [58]. Comparable core–shell structures have also been reported in other magnetized materials, such as Fe_3O_4/perlite@SiO_2 [59], where Fe_3O_4 acts as the magnetic core.

After phosphate adsorption, the FE-SEM images of M-COS-CSH revealed denser agglomerations of spherical and faceted clusters (Fig. 2d–f), likely associated with the formation of Ca—P products on the surface and within the pores of the composite. Acicular structures characteristic of HAP ($Ca_5(PO_4)_3OH$) were observed, consistent with previous findings [15]. Crystallization of carbonate HAP phases was also evident, appearing as coalesced rhombohedral crystals [60], while some calcium HAP formed plate-like morphologies [61]. Typically, spherical amorphous calcium phosphate (ACP) is the initial Ca—P precipitate that forms under saturation conditions, later transforming into hydroxyapatite (HAP) after 6–8 h of adsorption [7,27,62]. In contrast, HAP formation in this study was observed as early as 45 min. This rapid transformation aligns with previous reports of HAP formation after 2 h [15] and may be attributed to the elevated pH conditions, which are known to favor the formation of plate-like HAP structures [61].

The N_2 adsorption–desorption isotherm of M-COS-CSH exhibited a Type IV profile with H3 hysteresis loops (Fig. 3a), as classified by IUPAC, indicating a mesoporous structure composed of non-rigid aggregates of plate-like particles with slit-shaped pores. The presence of macropores, which may be inferred from the hysteresis loop, could further facilitate phosphate diffusion and enhance adsorption efficiency. These results are consistent with previous reports on magnetized CSH without COS [58], suggesting that COS incorporation does not alter the pore type within the nanocomposite. The pore size distribution (inset of Fig. 3a) ranged from 3 to 50 nm, with an average diameter of 4.063 nm. The BET surface area (S_{BET}) was 102.594 $m^2\ g^{-1}$, and the total pore volume was 0.370 $cm^3\ g^{-1}$. This surface area is significantly higher than magnetized CSH materials prepared by dynamic hydrothermal methods (66.8–77.1 $m^2\ g^{-1}$) [48]. Although it is lower than the 196 $m^2\ g^{-1}$ reported for magnetized CSH prepared through a complex, multistep hydrothermal process involving extended reaction and drying times (~19 h) [58], the M-COS-CSH developed in this study was synthesized through a much simpler and faster route, completed in under 5.2 h. Notably, increasing the amount of $FeCl_3$ from 7.56 g to 10.8 g resulted in a slight increase in surface area, from 102.594 $m^2\ g^{-1}$ to 106.520 $m^2\ g^{-1}$, suggesting a possible trade-off between magnetite content and available surface area.

After phosphate adsorption (Fig. 3b), the M-COS-CSH nanocomposite exhibited a 27 % increase in cumulative pore volume (0.510 $cm^3\ g^{-1}$) and a 32.49 % increase in S_{BET} (135.929 $m^2\ g^{-1}$). This increase in surface area and porosity may be attributed to the formation of porous calcium phosphate (Ca—P) products on the material's surface. The pore size distribution also followed a similar trend, although the average pore diameter slightly decreased to 3.636 nm. This reduction suggests that Ca—P products preferentially formed within the larger pores of M-COS-CSH, leading to a decrease in volume at those pore sizes. Notably, pores

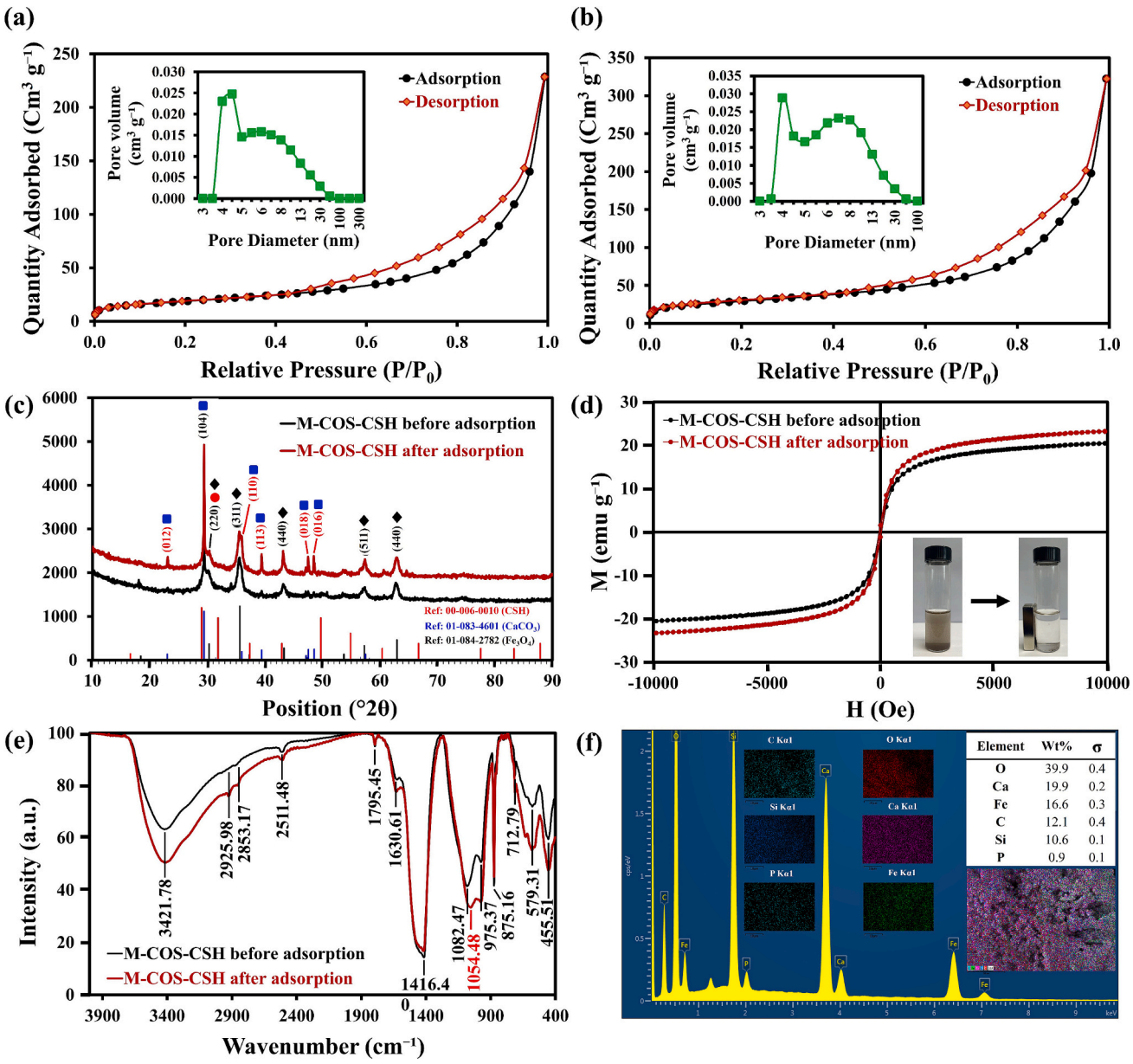

Fig. 3. Characterization of M-COS-CSH: (a) N_2 adsorption–desorption isotherm and pore size distribution before phosphate adsorption; (b) N_2 adsorption–desorption isotherm and pore size distribution after phosphate adsorption; (c) XRD pattern; (d) VSM curve; (e) FTIR spectra; and (f) EDX spectrum and elemental mapping after phosphate adsorption.

in the range of 200–300 nm were no longer present after adsorption, which supports the interpretation that these larger pores were filled or blocked by Ca—P precipitates.

The X-ray powder diffraction (XRD) pattern of M-COS-CSH nanoparticles is shown in Fig. 3c. Prominent diffraction peaks appeared at 29.4°, 30.2°, 35.5°, 43.1°, 57.3°, and 62.7°, corresponding to characteristic peaks of CSH, COS, and Fe_3O_4, as detailed in Supplementary Fig. S5. The diffraction peak at 29.4° is attributed to the (104) plane of calcite ($CaCO_3$), which likely formed due to the unavoidable reaction of COS with atmospheric CO_2 during synthesis [7,27] or possibly due to incomplete calcination of oyster shells [63,64]. This peak may also overlap with the (220) plane of tobermorite ($Ca_5Si_6O_{16}(OH)_2{\cdot}4H_2O$), which is typically observed around 29.3° in synthesized CSH [7,65]. A shoulder peak at 30.2° corresponds to the (220) reflection of Fe_3O_4, while the peaks at 35.5°, 43.1°, 57.3°, and 62.7° are assigned to the (311), (400), (511), and (440) planes of Fe_3O_4, respectively [46,66,67]. It is noteworthy that the peak at 43.1° could also reflect the presence of calcite or the (036) plane of tobermorite [7,65].

Following phosphate adsorption, most diffraction peaks remained consistent with those of the pristine M-COS-CSH, although the intensities of several peaks increased, indicating the formation of calcium phosphate phases. A sharper peak emerged at 23.1°, which was assigned to the (012) plane of calcite [39], while the intensity of the (104) peak at 29.4° also increased. Additional peaks at 36.0°, 39.4°, 47.5°, and 48.5° correspond to the characteristic reflections of $CaCO_3$ (JCPDS file no. 83–0577), with specific planes indexed as 35.9° (110), 39.4° (113), 47.6° (018), and 48.4° (116) [7,27,68–70]. Although the formation of ACP is typically indicated by a broad hump around $2\theta \approx 30°$ [71,72], this feature was not clearly distinguishable in the current XRD pattern. Several diffraction peaks were observed at positions consistent with those previously reported for brushite ($CaHPO_4{\cdot}2H_2O$), including $2\theta =$ 23.1°, 29.4°, 30.3°, 35.5°, 36.0°, 39.4°, 47.5°, and 48.5° [32]. However, no characteristic peaks of crystalline hydroxyapatite (HAP), typically found at $2\theta = 26.4°$, 31.9°, 32.2°, 32.9°, or 39.9° [15,71], were detected,

even though a HAP-like morphology was observed under FESEM.

The magnetic properties of M-COS-CSH before and after phosphate adsorption are shown in Fig. 3d. The material exhibited typical superparamagnetic behavior, with saturation magnetization (M_s) values of 20.367 emu g^{-1} before and 23.116 emu g^{-1} after phosphate adsorption. The observed increase in magnetization may be attributed to the influence of external magnetic fields or electrostatic interactions involving Ca—P species, which can enhance the magnetic response of the composite material [66]. The inset in Fig. 3d clearly demonstrates the magnetic separability of M-COS-CSH in aqueous solution using only a magnetic bar.

The functional groups of M-COS-CSH before and after phosphate adsorption were analyzed using FTIR spectroscopy (Fig. 3e). The spectra showed similar overall patterns, with notable increases in the intensities of several bands following phosphate adsorption. A broad absorption band around 3421 cm^{-1} was assigned to O—H stretching vibrations. This band showed increased intensity after adsorption, which is consistent with previous reports [7,25,39] and may indicate the formation of HAP ($Ca_5(PO_4)_3(OH)$) due to its O—H moiety [73]. A new peak appearing at 1055 cm^{-1} was attributed to the asymmetric stretching vibration (ν_3) of $H_2PO_4^-$ and HPO_4^{2-} groups, confirming the presence of Ca—P species. This suggests that $Ca(H_2PO_4)_2$ and $CaHPO_4$ were the predominant phosphate forms adsorbed onto the composite. This observation aligns with previously reported phosphate-related bands observed at 1038 cm^{-1} [48], 1046 cm^{-1} [27], and within the general range of 1000–1100 cm^{-1} [74,75]. Stretching vibrations of C—H in $–CH_2$ groups were identified at 2853–2926 cm^{-1} [66], while a band at 2511 cm^{-1} corresponded to O—H stretching [73]. The band at ~1633 cm^{-1} was assigned to H–O–H bending vibrations from water molecules [7]. A strong peak at 1416 cm^{-1} was assigned to the asymmetric stretching of CO_3^{2-} groups [76–78], commonly present in both COS and CSH. The peak may also involve the C—N stretching vibration of aromatic amines possibly originating from COS, as previously observed in KOH-activated crab carapace [77]. Other characteristic peaks of $CaCO_3$ were also observed at 875, 1795, and 2511 cm^{-1} [25]. A sharp band at 1083 cm^{-1} in the spectrum before phosphate adsorption, assigned to Si–O–Si stretching [15], appeared to overlap with the phosphate peak at 1055 cm^{-1} after adsorption. Similarly, the band at ~975 cm^{-1}, attributed to Si—O stretching [15], may overlap with P—O vibrations from PO_4^{3-} groups, typically observed around 963 cm^{-1} [36]. The peak at 713 cm^{-1} corresponded to Ca—O bond vibrations, confirming the presence of CaO in both COS and M-COS-CSH [25]. Finally, the peak at 579 cm^{-1} was attributed to Fe—O bond vibrations [66], which overlapped with the O–P–O asymmetric deformation near 571 cm^{-1} [25], resulting in an intensified signal observed at 581 cm^{-1}. The characteristic peaks of CSH, COS, and Fe_3O_4 were also analyzed and are presented in Supplementary Fig. S6.

The presence of Ca—P species after phosphate adsorption was confirmed by EDX analysis and elemental mapping (Fig. 3f). The results showed that P was present in the M-COS-CSH sample after adsorption at 0.9 ± 0.1 %, alongside other constituent elements such as Ca, O, Si, and Fe. Moreover, elemental mapping revealed a homogeneous distribution of P across the material, suggesting uniform phosphate adsorption over the M-COS-CSH surface.

XPS analysis of M-COS-CSH (Fig. 4) confirmed the successful adsorption of phosphate, as evidenced by the appearance of phosphorus-related peaks. The survey spectrum of M-COS-CSH before phosphate adsorption (Fig. 4a) revealed peaks corresponding to Si 2p (101.4 eV), C 1s (283.8 eV), Ca 2p (346.2 eV), O 1s (531.0 eV), and Fe 2p (711.8 eV), with oxygen being the dominant surface element, accounting for 52.2 at. %. Following phosphate adsorption, the binding energies of Ca 2p and Fe 2p shifted slightly to 347.0 eV and 709.4 eV, respectively, while other elemental peaks remained relatively unchanged. Moreover, an increase in the atomic percentages of Ca 2p (12.1 % to 12.3 %) and O 1s (52.2 % to 56.7 %) was observed (Fig. 4a), whereas the intensities of other deconvoluted peaks decreased. These changes suggest that phosphate

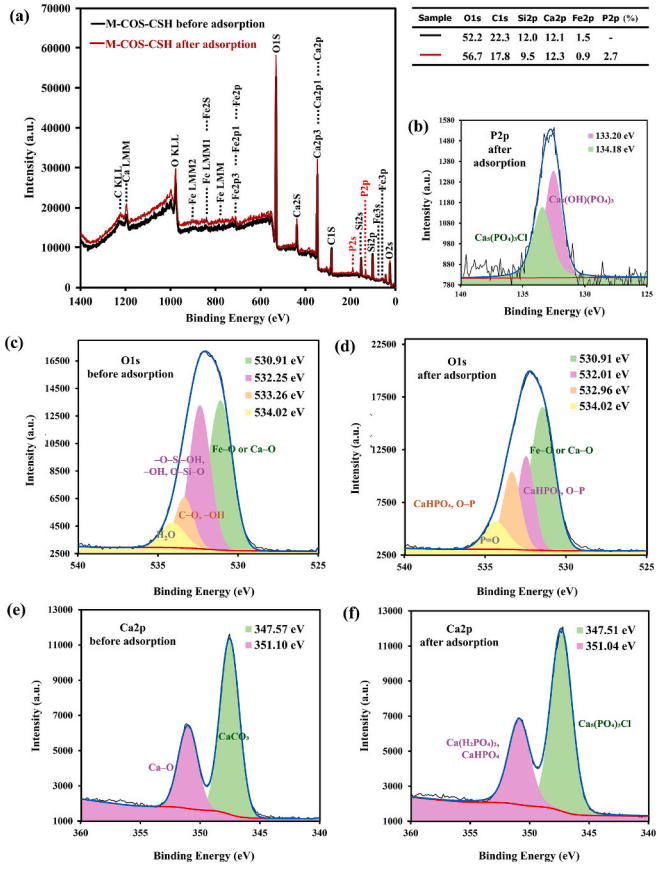

Fig. 4. X-ray photoelectron spectroscopy (XPS) spectra and peak deconvolution of M-COS-CSH: (a) survey spectrum; (b) P 2p; (c) O 1s before adsorption; (d) O 1s after adsorption; (e) Ca 2p before adsorption; and (f) Ca 2p after adsorption.

species interacted primarily with calcium and oxygen atoms on the M-COS-CSH surface during adsorption. Notably, a new P 2p peak appeared at 131.8 eV, accounting for 2.7 % atomic concentration. The deconvoluted P 2p spectrum (Fig. 4b) showed two distinct peaks at 133.20 and 134.18 eV. The first peak was assigned to $Ca_5(OH)(PO_4)_3$ (HAP) or $CaHPO_4$ [39,79], while the second peak corresponded to $Ca_5(PO_4)_3Cl$ [15,79,80], further confirming the formation of Ca—P species. The O 1s spectrum (Fig. 4c) was deconvoluted into four components, each corresponding to different oxygen environments. The peak at 530.91 eV was attributed to Fe—O or Ca—O bonds [48,79,81], while the peak at 532.25 eV was assigned to oxygen in silanol groups (–O–Si–OH), hydroxyl groups, or siloxane linkages (O–Si–O) [48,82]. The third component at 533.26 eV was attributed to C—O bonds or hydroxide species [79,82], and the final peak at 534.02 eV was associated with bound water [82]. After phosphate adsorption (Fig. 4d), the intensity of the 530.91 eV peak increased, which could be due to the formation of P—O bonds interacting with Fe—O or Ca—O bonds [79,81,83]. Two additional peaks emerged at 532.01 and 532.96 eV, corresponding to $CaHPO_4$ or HAP and O—P bonds, respectively [79,80,83,84]. The peak at 534.02 eV also showed a slight increase in intensity, possibly resulting from the contribution of P═O groups associated with HAP [84]. The Ca 2p spectrum displayed two main peaks both before and after phosphate adsorption. Prior to adsorption (Fig. 4e), peaks at 347.57 and 351.10 eV were assigned to Ca $2p_{3/2}$ and Ca $2p_{1/2}$, corresponding to $CaCO_3$ [85] and Ca—O [79], respectively. After phosphate adsorption (Fig. 4f), these peaks shifted slightly to 347.51 and 351.04 eV, consistent with the formation of Ca—P species such as $Ca(H_2PO_4)_2$, $CaHPO_4$, $Ca_5(PO_4)_3Cl$, or HAP [15,79,86,87].

3.3. Influence of adsorption conditions

A BBD was employed to evaluate four independent variables: A—adsorbent dose (g), B—initial phosphate concentration (mg L^{-1}), C—contact time (min), and D—pH. A total of 27 experimental runs, including three replicates at the center point (C = 3), were conducted to assess the experimental error and reproducibility of the data. The resulting RE values ranged from 21.58 % to 97.58 %. A quadratic polynomial model was then fitted to the data, yielding predicted %RE values ranging between 24.02 % and 98.73 % (Table 1). The final model is expressed in Eq. (2), where positive coefficients denote synergistic effects and negative coefficients indicate antagonistic interactions, in line with observations from the CCD model discussed earlier. The correlation between the experimental and predicted %RE values is presented in Supplementary Fig. S7a.

$$\begin{aligned}\text{Removal efficiency }(\%) = {} & 92.56 + 24.46A - 9.35B + 5.64C - 8.19D \\ & + 9.56AB - 0.86\,AC + 6.56\,AD \\ & + 5.18\,BC - 5.26BD \\ & + 6.93CD - 20.23A^2 - 4.94B^2 - 2.85C^2 - 6.05D^2\end{aligned} \quad (2)$$

The model exhibited strong statistical performance with an R^2 value of 0.9686, indicating excellent agreement between experimental and predicted data. The adjusted R^2 of 0.9319 indicates that the model explains approximately 93.19 % of the variability observed in %RE. The predicted R^2 value of 0.8208 was reasonably close to the adjusted R^2, with a difference below 0.2—within the generally accepted threshold for model consistency [53,54]. Additionally, the lack-of-fit F-value of 12.73, determined from ANOVA (Supplementary Table S5), was not statistically significant when compared to the pure error, thereby supporting the adequacy of the model.

The individual effects of each variable are illustrated in Supplementary Fig. S8. The profiler plot for adsorbent dose (Supplementary Fig. S8a) showed a positive correlation between dose and RE from 20 to 60 mg, likely due to the increased number of active sites available for phosphate adsorption [15,52]. However, RE reached a plateau between 60 and 80 mg and subsequently declined beyond 80 mg. This decline may be attributed to mass transfer limitations within the confined volume and particle agglomeration at high dosages, both of which reduce the effective surface area available for adsorption [36,52]. These results are consistent with findings from other studies that employed conventional optimization methods under similar experimental conditions [15,52].

Regarding initial phosphate concentration (Supplementary Fig. S8b), a gradual decrease in RE was observed with increasing phosphate levels. This trend is likely attributed to the saturation of available active adsorption sites at higher solute concentrations [88].

Contact time exhibited a modest influence on phosphate removal, with RE increasing slightly as contact time was extended from 15 to 75 min (Supplementary Fig. S8c). The perturbation plot (Supplementary Fig. S7b) suggested that the optimal RE occurred at the central coded level, corresponding to 45 min. This observation was supported by preliminary experiments, in which a 45-min contact time yielded a high RE of 98.06 % ± 0.19 % and adsorption capacity (Q_e) of 16.34 ± 0.03 mg g^{-1} at an initial phosphate concentration of 10 mg L^{-1} phosphate. In contrast, prolonged contact (1440 min) resulted in lower RE of 57.80 % ± 0.23 % and Q_e of 15.69 ± 0.06 mg g^{-1}, potentially due to desorption or competition with ions released from the adsorbent over time.

The solution pH also significantly influenced phosphate adsorption. RSM optimization revealed that higher RE occurred at acidic to neutral pH values, while efficiency declined under alkaline conditions (Supplementary Fig. S8d). This behavior is attributed to increased electrostatic repulsion between negatively charged phosphate species and the negatively charged M-COS-CSH surface at elevated pH. In practice, the pH of both synthetic and real wastewater samples ranged from 7.15 to 8.45, while the point of zero charge (pH_{PZC}) for M-COS-CSH was determined to be 8.75 (Supplementary Fig. S9). At pH values below pH_{PZC}, the M-COS-CSH surface becomes positively charged, facilitating electrostatic attraction with phosphate anions such as $H_2PO_4^-$ and HPO_4^{2-}—the dominant species at typical environmental pH values [89]. Maximum phosphate removal occurred within the pH range of 5 to 7. Calcium ions (Ca^{2+}) present in M-COS-CSH likely contribute to initial electrostatic interactions with phosphate species, followed by the formation of calcium phosphate precipitates. The incorporation of COS into the CSH-based magnetic nanocomposite likely enhances the surface density of Ca^{2+}, thereby increasing the positive surface charge and improving adsorption performance at pH < pH_{PZC} [90]. At pH above pH_{PZC} (pH > 8.57), the surface becomes increasingly negative, reducing adsorption efficiency due to enhanced electrostatic repulsion. After 45 min of adsorption, the solution pH stabilized around 9–10, which is attributed to the release of OH^- ions from the CSH component [7,15]. This pH shift may further inhibit phosphate adsorption; however, high-pH conditions can also promote HAP precipitation, making its formation plausible in the later stages of the process [31,77,91,92].

The combined effect of all four independent variables at their central coded levels is summarized in Supplementary Fig. S7b. Among these variables, adsorbent dose exhibited the greatest influence on phosphate removal, as indicated by the steepest response slope. Initial phosphate concentration and pH had moderate effects, whereas contact time exerted the least influence. Fig. 1b–g present contour and three-dimensional response surface plots illustrating the interactive effects of variable pairs on phosphate adsorption by M-COS-CSH. The highest RE was achieved under the central experimental conditions: 60 mg of M-COS-CSH, 10 mg L^{-1} phosphate, 45 min of contact time, and pH 6.28. Under these optimized parameters, the model predicted a theoretical maximum RE of 97.30 %. It is noteworthy that the pH of real wastewater samples ranged from 7.15 to 8.45, and only a minimal influence of pH was observed within the acidic to neutral range. Therefore, pH adjustment is likely unnecessary for practical applications. When the optimized conditions were applied without pH adjustment (pH = 6.84), RE of 98.06 % ± 0.19 % (using cellulose acetate syringe filtration) and 95.86 % ± 1.11 % (using magnetic separation) were obtained.

3.4. Isotherm, kinetic, and thermodynamic analysis

The adsorption isotherm was studied using initial phosphate concentrations ranging from 5 to 100 mg L^{-1}. As shown in Fig. 5a, RE gradually declined from 94.27 % ± 0.53 % to 69.00 % ± 2.47 % with increasing concentration, while Q_e increased from 7.86 ± 0.04 to 163.86 ± 4.05 mg g^{-1}. These results indicate that M-COS-CSH achieves higher RE at lower phosphate concentrations, which is consistent with the RSM findings. To elucidate the adsorption mechanism, the experimental data were fitted to Langmuir, Freundlich, Sips, and Dubinin-Radushkevich (D-R) isotherm models (Figs. 5b–e). Model performance was assessed using R^2, sum of squared errors (SSE), and residual standard deviation (SD). Among the models, the Langmuir isotherm provided the best fit, showing the highest R^2 and lowest SSE and SD values. This suggests that phosphate adsorption onto M-COS-CSH follows a monolayer adsorption mechanism on a homogeneous surface with uniform binding sites, which aligns with previous findings for CSH [15,27,29] and COS [25]. These results indicate that the nanocomposite largely retains the key adsorption characteristics of both active materials. Furthermore, the dimensionless separation factor (R_L), calculated according to previous literature [7], ranged from 0.05 to 0.53, confirming that the adsorption process was favorable ($0 < R_L < 1$). This is also in good agreement with previous studies on phosphate adsorption onto CSH- and COS-based materials [15,25].

The maximum adsorption capacity (Q_m) of M-COS-CSH was determined to be 161.29 mg g^{-1}, demonstrating its excellent potential for phosphate adsorption. This performance surpasses that of many previously reported materials, including those derived from shell waste

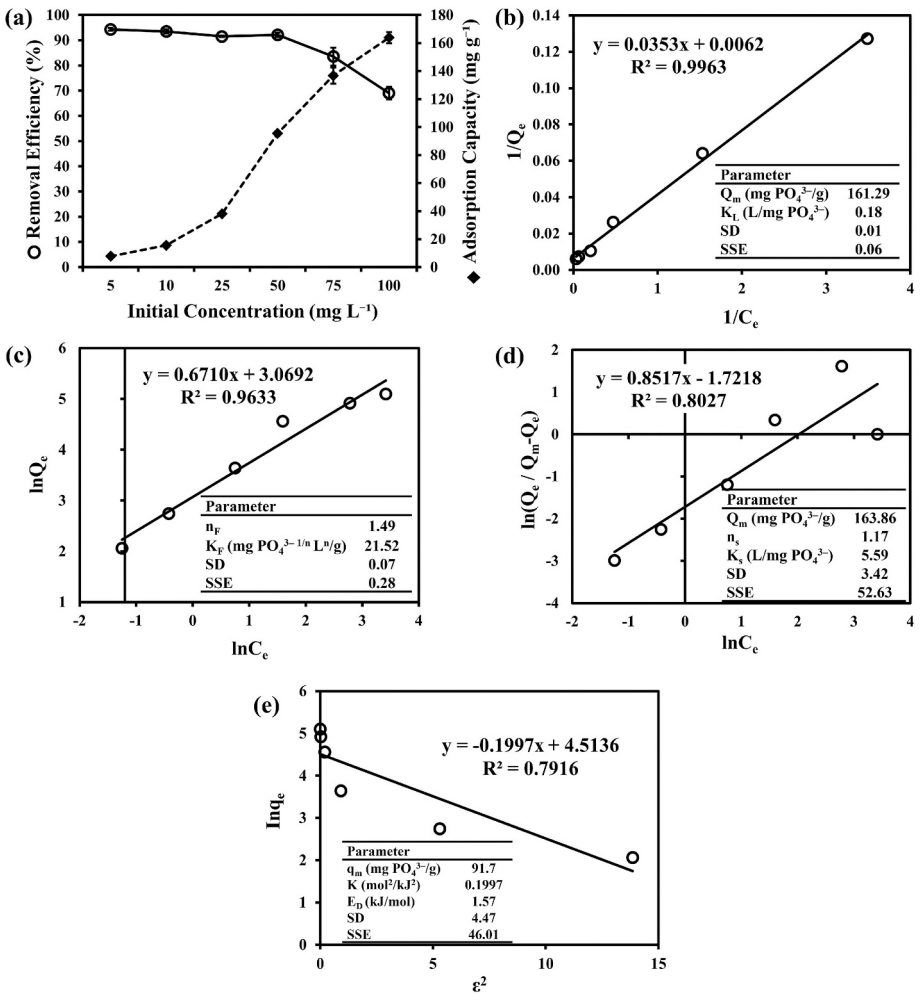

Fig. 5. (a) Effect of initial phosphate concentration on removal efficiency and adsorption capacity of M-COS-CSH. Adsorption isotherm plots fitted with (b) Langmuir, (c) Freundlich, (d) Sips, and (e) Dubinin–Radushkevich models. Experimental conditions: 0.06 g M-COS-CSH in 100 mL phosphate solution (5–100 mg L^{-1}), without pH adjustment; contact time: 45 min; temperature: 25 °C.

Table 2
Maximum phosphate adsorption capacities and preparation times of various materials based on shell waste and calcium silicate hydrate.

Adsorbent	Preparation time	Contact time	Temperature (K)	Q_{max} (mg g^{-1})	Ref.
Shell materials					
Mussel shells	2 days	144 h	298	0.8	[102]
Calcined oyster shells	2.5 h	240 min	298	5.3	[41]
Biochar composite oyster shells	26.5 h	200 min	298	146.3	[103]
Snail shells	2 days	60 min	303	62.5–66.7	[37]
Whelk and scallop shells	3 h	420 min	298	8.8–9.5	[33]
Fe and La co-modified clam shells	3.1 h	20 min	298	43.6	[104]
CSH materials					
CSH composite from waste glass and scallop shell	24 h	120 h	298	73.0	[105]
CSH from blast furnace slag	8.2 h	24 h	298	53.1	[106]
Fe_3O_4@CSH	15.9 h	24 h	298	55.8	[48]
CSH from electrolytic manganese residue	12 h	465 min	298–308	65.8–85.5	[107]
CSH prepared under ultrasound	1.2 h	120 min	298	109.4	[27]
CSH from solid waste residue	26 h	90 min	318	82.6	[108]
CSH composite from CaO and Polonite under hydrothermal	16 h	60 min	308	>18	[109]
M-COS-CSH	5.2 h	45 min	298	161.3	This work

(0.8–66.7 mg g^{-1}), CSH (53.1–109.4 mg g^{-1}), and their composites (18–146.3 mg g^{-1}), as summarized in Table 2. In addition to its high adsorption capacity, M-COS-CSH offers advantages in both synthesis and kinetics. The material requires only 5.2 h to synthesize, compared to 1.2 h to 2 days for similar adsorbents, and reaches adsorption equilibrium within 45 min significantly faster than the 20 min to 144 h reported for other materials. These features make M-COS-CSH a highly promising candidate for efficient phosphate removal and recovery in practical water treatment applications.

Kinetic studies were performed over contact times ranging from 5 to 60 min and temperatures from 298 to 318 K (Supplementary Fig. S10). The adsorption process was rapid, achieving 82.26 % ± 3.42 % removal

within the first 5 min at 298 K, likely due to the high availability of active adsorption sites and strong electrostatic interactions between calcium and phosphate ions. The RE continued to increase, reaching 94.18 % ± 0.14 % at 45 min, before slightly declining to 93.93 % ± 0.53 % at 60 min. A similar trend was observed in Q_e, which increased from 13.71 ± 0.57 to 15.70 ± 0.02 mg g^{-1} between 5 and 45 min, then plateaued at 15.66 ± 0.09 mg g^{-1} at 60 min. These results align well with the RSM findings. The kinetic data were fitted to pseudo-first-order, pseudo-second-order, and intra-particle diffusion models (Table 3). Among these, the pseudo-second-order model provided the best fit, with R^2 values ranging from 0.9997 to 1.0000 across the studied temperatures This suggests that phosphate adsorption onto M-COS-CSH closely follows pseudo-second-order kinetics. Moreover, the estimated Q_e value from the pseudo-second-order model at 298 K (15.873 mg g^{-1}) closely matched the experimental Q_e (15.70 ± 0.02 mg g^{-1}), further confirming the model's suitability for describing the adsorption kinetics. These results are consistent with previous studies involving CSH nanoparticles [25,27,29], PVA-CSH composites [15,29], and COS-based materials [25], which also reported phosphate removal behavior well described by the pseudo-second-order model. The rate constant (k_2) increased from 0.087 to 0.142 g mg^{-1} min^{-1}, and the Q_e rose from 15.873 to 16.077 mg g^{-1} as the temperature increased from 298 to 308 K, indicating an endothermic adsorption process.

Thermodynamic parameters were also evaluated to further elucidate the nature of the adsorption process. The Gibbs free energy change (ΔG°) ranged from −9.97 to −10.84 kJ mol^{-1}, confirming the spontaneous nature of phosphate adsorption onto M-COS-CSH. The enthalpy change (ΔH°) was 3.00 kJ mol^{-1} and the entropy change (ΔS°) was 43.52 J mol^{-1} K^{-1}, indicating that the process is endothermic and becomes more favorable at higher temperatures [7,29,48]. The positive ΔS° value also suggests increased randomness at the solid–liquid interface during adsorption, likely due to the release of ions from the surface sites.

3.5. Effect of coexisting ions on phosphate adsorption

To evaluate the effect of potential coexisting ions—NO_3^-, NO_2^-, SO_4^{2-}, CO_3^{2-}, HCO_3^-, F^-, and Cl^-—on phosphate adsorption by M-COS-CSH, competitive adsorption experiments were conducted. The results (Table 4) demonstrated that even when coexisting anions were present at concentrations 50 times higher than that of phosphate, the change in phosphate RE was less than 5 %, indicating minimal interference with adsorption performance. Specifically, NO_3^-, NO_2^-, and Cl^- had negligible effects, likely due to their tendency to be non-specifically adsorbed via outer-sphere surface complexation, as previously observed in KOH-activated crab carapace materials [25,77]. Among the tested ions, CO_3^{2-} and HCO_3^- exhibited the most significant impact on phosphate adsorption, particularly when their concentrations were fivefold higher than that of phosphate. This effect is attributed to the pH increase induced by CO_3^{2-}, which negatively affects phosphate adsorption, as previously discussed and reported [15,93]. A similar trend was observed with HCO_3^-, the hydrolyzed form of CO_3^{2-}. These anions may compete with phosphate for active sorption sites and may also interact with phosphate to form inner-sphere complexes, thereby reducing phosphate uptake [15,92,94].

In a mixed-ion system where all coexisting anions were present at fivefold concentrations relative to phosphate, the removal efficiency remained high at 93.58 % ± 0.32 %, with only a − 3.39 % ± 0.53 % change. These results highlight the excellent selectivity and robustness of M-COS-CSH for phosphate removal, even in complex water matrices. It is also noteworthy that in actual WWTP effluents, the concentrations of these competing anions are typically much lower than those used in this study, and therefore are unlikely to significantly affect phosphate adsorption efficiency.

Table 3
Kinetic model parameters for phosphate adsorption onto M-COS-CSH.

Model	Temperature (K)	Parameter	M-COS-CSH
Pseudo-first-order	298	Q_e (mg g^{-1})	1.626
		k_1 (min^{-1})	0.049
		R^2	0.5421
	308	Q_e (mg g^{-1})	0.429
		k_1 (min^{-1})	0.011
		R^2	0.0298
	318	Q_e (mg g^{-1})	0.111
		k_1 (min^{-1})	0.003
		R^2	0.0012
Pseudo-second-order	298	Q_e (mg g^{-1})	15.873
		k_2 (g mg^{-1} min^{-1})	0.087
		R^2	1
	308	Q_e (mg g^{-1})	16.026
		k_2 (g mg^{-1} min^{-1})	0.122
		R^2	0.9999
	318	Q_e (mg g^{-1})	16.077
		k_2 (g mg^{-1} min^{-1})	0.142
		R^2	0.9997
Intra-particle diffusion	298	k_p (mg g^{-1} $min^{-1/2}$)	0.308
		C (mg g^{-1})	13.597
		R^2	0.758
	308	k_p (mg g^{-1} $min^{-1/2}$)	0.223
		C (mg g^{-1})	14.381
		R^2	0.6724
	318	k_p (mg g^{-1} $min^{-1/2}$)	0.221
		C (mg g^{-1})	14.341
		R^2	0.8445

Table 4
Effect of coexisting anions on phosphate removal efficiency.

Anion	Concentration (mg L^{-1})	pH initial	%Change in RE
NO_3^-	2500	7.15	−3.66 ± 0.81
NO_2^-	1000	7.46	5.38 ± 0.00
Cl^-	1000	7.60	−1.53 ± 0.27
SO_4^{2-}	500	7.56	−3.03 ± 1.01
F^-	500	7.34	5.06 ± 0.03
CO_3^{2-}	50	10.73	−2.82 ± 0.37
HCO_3^-	50	8.34	−1.22 ± 0.47
Mix anions	50	10.27	−3.39 ± 0.53

(phosphate concentration: 10 mg L^{-1})

3.6. Phosphate adsorption mechanism on M-COS-CSH

The phosphate adsorption mechanism onto M-COS-CSH was elucidated through a combination of characterization techniques. EDX analysis confirmed the presence of P on the M-COS-CSH surface after adsorption, while elemental mapping revealed a uniform P distribution throughout the material, indicating effective surface coverage. XPS analysis further supported these findings, with the emergence of a new P 2p peak at 131.8 eV and an atomic concentration of 2.7 %, confirming phosphate incorporation. Deconvolution of the P 2p spectrum revealed two distinct peaks at 133.20 eV and 134.18 eV, corresponding to calcium phosphate species such as $Ca_5(OH)(PO_4)_3$ (HAP), $CaHPO_4$, and $Ca_5(PO_4)_3Cl$ [15,39,79,80]. In the O 1s region, two new peaks at 532.01 eV and 532.96 eV were observed after adsorption, attributed to P—O bonds and phosphate-containing phases, respectively [80,83,84]. These XPS results are consistent with the post-adsorption XRD pattern, where diffraction peaks at 2θ = 23.1°, 29.4°, 30.3°, 35.5°, 36.0°, 39.4°, 47.5°, and 48.5° matched those of brushite ($CaHPO_4{\cdot}2H_2O$) [32]. FTIR spectra further confirmed the formation of phosphate species, with the emergence of a distinct peak at 1055 cm^{-1}, attributed to the asymmetric stretching vibration (ν_3) of $H_2PO_4^-$ and HPO_4^{2-}, suggesting the presence of $Ca(H_2PO_4)_2$ and $CaHPO_4$ on the material surface [27,48,75,95]. Additionally, FESEM imaging revealed the development of needle-like (acicular) structures typically associated with HAP ($Ca_5(PO_4)_3OH$), coalesced rhombohedral crystals of carbonated HAP, and plate-like morphologies of various calcium phosphate phases [60,61].

These morphological features, along with the observed spectral and crystallographic changes, indicate that surface microprecipitation was the dominant mechanism for phosphate removal. Phosphate removal likely proceeded via the following reactions involving calcium (Ca^{2+}) and hydroxide (OH^-) ions released from the COS and CSH components, leading to the formation of various calcium phosphate precipitates, as illustrated in Eqs. (3)–(5) [15,29,39,79,96,97].

$$Ca^{2+} + HPO_4^{2-} \rightarrow CaHPO_4\ (Brushite) \quad (3)$$

$$Ca^{2+} + H_2PO_4^- \rightarrow Ca(H_2PO_4)_2 \quad (4)$$

$$5Ca^{2+} + 3HPO_4^{2-} + 4OH^- \rightarrow Ca_5(PO_4)_3OH\ (HAP) + 3H_2O \quad (5)$$

$$5Ca^{2+} + 3HPO_4^{2-} + OH^- + Cl^- \rightarrow Ca_5(PO_4)_3Cl \quad (6)$$

The formation of $Ca_5(PO_4)_3Cl$ is particularly notable, as the CSH in M-COS-CSH was synthesized via co-precipitation under ultrasonic irradiation—a process in which Cl^-, likely originating from NaCl by-products, are present in the reaction medium [15]. These Cl^- ions may interact with Ca^{2+} and phosphate species to facilitate $Ca_5(PO_4)_3Cl$ formation, further supported by the P 2p XPS peak at 134.18 eV [15,79,80].

In addition to precipitation, ligand exchange via inner-sphere complexation also contributed to phosphate adsorption. This mechanism is supported by the presence of $CaCO_3$ in the adsorbent, as evidenced by a distinct peak at $2\theta = 29.4^\circ$ in the XRD pattern, corresponding to the (104) plane of calcite, and prominent FTIR bands at 875, 1416, 1795, and 2511 cm^{-1} [25,76–78]. These findings suggest that $CaCO_3$ originated from residual uncalcined oyster shells or from carbonation occurring during synthesis [7,27,63,64]. XPS analysis also confirmed the presence of $CaCO_3$, with Ca 2p peaks at 347.57 and 351.10 eV, corresponding to $CaCO_3$ and Ca—O bonds, respectively [15,79].

Phosphate ions likely underwent ligand exchange with surface ≡Ca–CO_3 groups, forming inner-sphere surface complexes through Lewis acid–base interactions, as illustrated in Eqs. (7) and (8) [15,25]:

$$\equiv Ca - CO_3 + H_2PO_4^- + H_2O \rightarrow \equiv Ca - H_2PO_4 + HCO_3^- + OH^- \quad (7)$$

$$\equiv Ca - CO_3 + HPO_4^{2-} + H_2O \rightarrow \equiv Ca - HPO_4 + HCO_3^- + OH^- \quad (8)$$

These interactions may result in the formation of mononuclear monodentate or bidentate surface complexes, result in phosphate species bind to one or two calcium centers, respectively [15,85,96,97].

Additionally, previous studies have suggested that high desorption efficiencies using 0.5 M HCl indicate that inner-sphere complexation and surface precipitation are the dominant adsorption mechanisms [77]. In this study, desorption experiments with 0.1 M and 0.5 M HCl yielded excellent phosphate RE of 95.75 % ± 0.62 % and 106.42 % ± 2.91 %, respectively, suggesting near-complete desorption of adsorbed phosphate. These findings further support the conclusion that inner-sphere complexation and surface precipitation are the primary mechanisms governing phosphate adsorption onto M-COS-CSH. The proposed adsorption mechanisms are schematically illustrated in Fig. 2g.

3.7. Real sample applications

The M-COS-CSH adsorbent was applied to remove phosphate from 10 real water samples collected from Phuket, Thailand. The initial phosphate concentrations in these samples, measured by spectrophotometry, ranged from 0.02 to 32.96 mg L^{-1} (Table 5). Five samples (Sample 6 to 10) with low phosphate levels (< 0.5 mg L^{-1}) were spiked with a phosphate standard prior to treatment with M-COS-CSH. The RE ranged from 70.81 % ± 2.47 % to 94.24 % ± 0.39 %, demonstrating the strong potential of M-COS-CSH for real-world applications. Seawater samples exhibited relatively lower RE than wastewater, likely due to the presence of high chloride concentrations (up to 19,350 mg L^{-1} [98]) which can interfere with phosphate adsorption on M-COS-CSH. Furthermore, the treated water met Thailand's discharge effluent standards, with COD and TSS values of 13.46 mg L^{-1} and 32.00 mg L^{-1}, respectively [14]. These results confirm the effectiveness of M-COS-CSH in removing phosphate and mitigating nutrient pollution in aquatic environments.

Additionally, the potential leaching of Fe^{2+} and Ca^{2+} ions from the adsorbent into the treated solution was evaluated, and the results are presented in Supplementary Table S6. The Fe^{2+} concentration showed minimal change compared to the initial solution (< +0.075 ± 0.10 mg L^{-1}), indicating negligible leaching across the tested pH range. In contrast, Ca^{2+} was released in the range of +37.693 ± 0.022 to +39.440 ± 0.137 mg L^{-1}. This behavior is consistent with previous studies on calcium-rich materials such as CSH and COS, where Ca^{2+} ions are known to leach into solution and subsequently form complexes with phosphate. In the present study, the relatively high Ca^{2+} concentrations observed—particularly in samples with low phosphate levels—suggest that limited ion–phosphate complexation occurred, resulting in the accumulation of free Ca^{2+} in the solution.

3.8. Reusability and stability of M-COS-CSH

The reusability of M-COS-CSH was evaluated using ultrapure water, HCl, and NaOH as regeneration solutions (Supplementary Fig. S11). The results indicated that both HCl and NaOH led to a significant reduction in adsorption efficiency in the second cycle, particularly at high NaOH concentration. This decline is likely due to the detrimental effects of these chemical agents on the adsorbent surface during the desorption process. Previous studies have reported that HCl disrupts ionic and hydrogen bonding interactions between oxygen atoms in $H_2PO_4^-$ and reactive metal and oxygen atoms on the adsorbent surface [99]. Such disruption weakens van der Waals forces, accelerates phosphorus desorption, and ultimately reduces adsorption capacity. Similarly, high concentrations of NaOH have been shown to degrade the structure of

Table 5
Phosphate removal efficiency and adsorption capacity of M-COS-CSH in real water samples.

Sample	Type	Concentration* (mg L^{-1})	pH initial	pH final	Removal efficiency (%)	Adsorption capacity (mg g^{-1})
1	Effluent from WWTP	17.44	7.42	9.63	91.79 ± 0.87	26.68 ± 0.25
2	Effluent from WWTP	7.47	8.19	9.70	90.72 ± 0.62	11.29 ± 0.08
3	RO concentrate	32.96	7.60	9.21	94.24 ± 0.39	51.77 ± 0.21
4	Wastewater	11.28	7.15	9.54	88.25 ± 0.76	16.59 ± 0.14
5	Wastewater	10.10	7.58	9.10	76.15 ± 0.66	12.82 ± 0.11
6	Coastal seawater	0.44	8.11	9.56	70.81 ± 2.47	18.46 ± 0.64
7	Coastal seawater	0.32	8.34	9.55	72.99 ± 1.75	19.41 ± 0.47
8	Coastal seawater	0.10	8.45	9.58	74.95 ± 1.80	19.13 ± 0.46
9	Open seawater	0.02	8.20	9.54	88.25 ± 0.76	16.59 ± 0.14
10	Coastal seawater	0.04	8.21	9.53	74.99 ± 3.22	17.64 ± 0.76

* Initial phosphate concentration. Experimental conditions: 100 mL water sample, 0.06 g M-COS-CSH, contact time of 45 min, room temperature, and no pH adjustment.

metal–organic frameworks (MOFs) by hydrolyzing metal–ligand bonds [100]. This process can result in structural collapse, loss of porosity, and altered surface chemistry, further diminishing adsorption performance. Among the tested regenerants, ultrapure water yielded the best regeneration performance. However, the removal efficiency decreased to 61.24 % ± 4.47 % in the second cycle. This decline may be attributed to incomplete phosphate desorption—with only 77.57 % of the adsorbed phosphate being recovered—partial saturation of active sites, or irreversible surface precipitation of calcium phosphate, which may block adsorption sites and hinder further uptake. Additionally, the third adsorption–desorption cycle exhibited a dramatic reduction in phosphate RE, further indicating a loss of active adsorption capacity. Despite the performance decline, the spent adsorbent retained its strong magnetic properties, allowing for easy recovery and handling. This magnetic recoverability is advantageous for practical applications, as it facilitates repeated use, reduces operational costs, and minimizes secondary waste generation. Future work may focus on optimizing mild and efficient regeneration strategies to enhance reusability without compromising structural stability.

Additionally, 0.1 and 0.5 M HCl—extractants previously reported for assessing plant-available phosphorus [101]—were applied to phosphate-loaded M-COS-CSH. The desorption efficiencies were 95.75 ± 0.62 % and 106.42 ± 2.91 %, respectively, indicating near-complete phosphate recovery. These findings suggest that the adsorbed phosphate is readily bioavailable, indicating that M-COS-CSH could be repurposed as a slow-release fertilizer. Therefore, phosphate-loaded M-COS-CSH holds promise for reuse in agriculture, supporting a zero-waste and circular-economy approach. This multifunctional performance underscores the material's potential for large-scale applications in eutrophication control while aligning with sustainable practices aimed at enhancing food and environmental security.

Furthermore, M-COS-CSH exhibited good storage stability when stored in a desiccator at room temperature. The phosphate RE declined by only 1.27 % and 2.49 % after two and five months of storage, respectively, compared to the freshly synthesized material. This excellent stability, combined with the material's strong magnetic properties and high phosphate recovery efficiency, underscores the potential of M-COS-CSH as a practical adsorbent for wastewater treatment and resource recovery applications.

3.9. Feasibility for practical applications based on continuous-flow system

To assess the practical applicability of M-COS-CSH, a preliminary continuous-flow experiment was conducted using a plastic column (1.0 cm inner diameter × 9.5 cm length), packed with approximately 1.4 g of M-COS-CSH powder to achieve a material bed height of 2.5 cm. A support layer consisting of gravel and wool was placed at both the top and bottom of the adsorbent bed (Supplementary Fig. S12a). Prior to phosphate loading, ultrapure water was passed through the column at a flow rate of 1 mL min^{-1} for 1 h to equilibrate the system and remove any potential impurities. Subsequently, a 10 mg L^{-1} phosphate solution was introduced in up-flow mode at the same flow rate (Supplementary Fig. S12c). A neodymium magnet was placed at the column outlet to prevent loss of M-COS-CSH particles (Supplementary Fig. S12b). The resulting breakthrough curve (Supplementary Fig. S13) demonstrated a phosphate RE of 98.91 % and an estimated adsorption capacity of 106.82 mg g^{-1}. The breakthrough time (t_b), defined as the time at which the effluent concentration reached 10 % of the influent concentration ($Ct/C_0 = 0.1$), was 6480 min, while the exhaustion time (t_e), corresponding to 90 % of the influent concentration ($Ct/C_0 = 0.9$), was 13,800 min. The mass transfer zone (MTZ) was estimated to be 1.33 cm, and the total volume of treated effluent (V_{eff}) was 15.12 L.

These findings demonstrate that M-COS-CSH exhibits excellent potential for implementation in continuous treatment processes, supporting its scalability and feasibility for practical water purification and phosphate recovery applications.

4. Conclusions

A magnetic nanocomposite (M-COS-CSH) was successfully developed from calcined oyster shell waste and calcium silicate hydrate via a simple, rapid synthesis process completed in just 5.2 h. The incorporation of magnetic properties enabled easy recovery of the adsorbent, while the material's intrinsic alkalinity minimized the need for post-treatment pH adjustment. Optimization using Response Surface Methodology (RSM) ensured high performance under practical conditions, achieving a maximum phosphate removal efficiency of 98.06 % ± 0.19 % and an adsorption capacity of 161.29 mg g^{-1} under neutral pH, indicating monolayer adsorption on a homogeneous surface. The adsorption behavior followed the Langmuir isotherm and pseudo-second-order kinetics. Comprehensive characterization and desorption experiments using strong acid revealed that surface microprecipitation and inner-sphere complexation were the predominant adsorption mechanisms. Importantly, M-COS-CSH demonstrated high selectivity and robustness in real water samples, with removal efficiencies ranging from 70.81 % ± 2.47 % to 94.24 % ± 0.39 %, and maintained performance in the presence of competing anions. Although regeneration efficiency declined gradually over multiple cycles, the material retained good magnetic recoverability, and the phosphate-loaded adsorbent showed promising potential for reuse as fertilizer—supporting sustainable resource recovery and a circular-economy approach.

From a technical and economic perspective, the use of low-cost oyster shell waste as a raw material significantly reduces the production cost of the adsorbent, while the material's high removal efficiency and stability in continuous-flow systems underscore its feasibility for scale-up and long-term application. The dual functionality of phosphate removal and nutrient recovery offers a cost-effective solution for wastewater treatment while simultaneously supporting agricultural resource recycling. In addition, the mitigation of eutrophication via this approach provides considerable environmental and economic benefits by protecting aquatic ecosystems and reducing downstream water treatment expenses.

To fully realize the practical implementation of M-COS-CSH, future research should focus on enhancing regeneration efficiency—potentially through surface modification strategies or the use of milder desorbing agents—and conducting pilot-scale investigations to evaluate long-term performance, scalability, and cost-effectiveness under diverse environmental conditions. Additionally, assessing the release kinetics of phosphate from spent adsorbent in soil environments will further support its application as a sustainable, slow-release fertilizer.

Overall, the findings highlight M-COS-CSH as a promising, cost-effective, and environmentally sustainable candidate for practical phosphate removal and recovery, aligning with the principles of circular economy and integrated water–agriculture resource management.

CRediT authorship contribution statement

Chanita Boonkanon: Writing – original draft, Visualization, Validation, Methodology, Investigation, Funding acquisition, Data curation. **Worawit Wongniramaikul:** Writing – review & editing, Validation, Methodology, Data curation, Conceptualization. **Chanadda Phawachalotorn:** Writing – review & editing, Validation, Data curation. **Somsak Limwongsakorn:** Resources, Data curation. **Aree Choodum:** Writing – review & editing, Writing – original draft, Supervision, Resources, Project administration, Methodology, Funding acquisition, Data curation, Conceptualization.

Declaration of competing interest

The authors declare that they have no known competing financial interests or personal relationships that could have appeared to influence the work reported in this paper.

Acknowledgements

This research was supported by the Postdoctoral Fellowship from Prince of Songkla University for C. Boonkanon.

Appendix A. Supplementary data

Supplementary data to this article can be found online at https://doi.org/10.1016/j.jwpe.2025.108421.

Data availability

Data will be made available on request.

References

[1] J. Dunn, M.H. Grider, Physiology, Adenosine Triphosphate, StatPearls, 2023. https://www.ncbi.nlm.nih.gov/books/NBK553175/. (Accessed 2 January 2025).
[2] J. Singh, J.S. Hundal, A. Sharma, U. Singh, A.P.S. Sethi, P. Singh, Phosphorus nutrition in dairy animals: A review, Int. J. Curr. Microbiol. App. Sci. 7 (04) (2018) 3518–3530.
[3] M. Gross, Where is all the phosphorus? Curr. Biol. 27 (21) (2017) R1141–R1144.
[4] T. Taweekarn, W. Wongniramaikul, P. Roop-o, W. Towanlong, A. Choodum, Recovering phosphate from complex wastewater using macroporous Cryogel composited calcium silicate hydrate nanoparticles, Molecules 29 (1) (2024) 228.
[5] H.M. Azam, S.T. Alam, M. Hasan, D.D.S. Yameogo, A.D. Kannan, A. Rahman, M. J. Kwon, Phosphorous in the environment: characteristics with distribution and effects, removal mechanisms, treatment technologies, and factors affecting recovery as minerals in natural and engineered systems, Environ. Sci. Pollut. Res. Int. 26 (20) (2019) 20183–20207.
[6] Y. Li, L. Fang, W. Yuanzhu, W. Mi, L. Ji, Z. Guixiang, P. Yang, Z. Chen, Y. Bi, Anthropogenic activities accelerated the evolution of river trophic status, Ecol. Indic. 136 (2022) 108584.
[7] T. Taweekarn, W. Wongniramaikul, A. Choodum, Removal and recovery of phosphate using a novel calcium silicate hydrate composite starch cryogel, J. Environ. Manag. 301 (2022) 113923.
[8] P. Sedyaaw, V.R. Bhatkar, A.N. Sawant, A review on effects of eutrophication in aquatic ecosystem, Int. J. Dev. Res. 14 (04) (2024) 65362–65369.
[9] H. Wang, J. Garcia Molinos, J. Heino, H. Zhang, P. Zhang, J. Xu, Eutrophication causes invertebrate biodiversity loss and decreases cross-taxon congruence across anthropogenically-disturbed lakes, Environ. Int. 153 (2021) 106494.
[10] B. BhagowatiK, U. Ahamad, A review on lake eutrophication dynamics and recent developments in lake modeling, Ecohydrol. Hydrobiol. 19 (1) (2019) 155–166.
[11] S. Chihoub, U. Christaki, S. Chelgham, R. Amara, Z. Ramdane, Z. Zebboudj, S. Rachik, E. Breton, Coastal eutrophication as a potential driver of functional homogenization of copepod species assemblages in the Mediterranean Sea, Ecol. Indic. 115 (2020) 106388.
[12] Y. Zhang, M. Li, J. Dong, H. Yang, L. Van Zwieten, H. Lu, A. Alshameri, Z. Zhan, X. Chen, X. Jiang, W. Xu, Y. Bao, H. Wang, A critical review of methods for analyzing freshwater eutrophication, Water 13 (2) (2021) 225.
[13] R. Prasertphon, P. Jitchum, R. Chaichana, Water chemistry, phytoplankton diversity and severe eutrophication with detection of microcystin contents in Thai tropical urban ponds, Appl. Ecol. Environ. Res. 18 (4) (2020) 5939–5951.
[14] The Ministry of Natural Resources and Environment of Thailand, Notification of the Ministry of Natural Resources and Environment for standard levels for discharge from municipal wastewater treatment plant. https://www.pcd.go.th/laws/4508/, 2010. (Accessed 8 January 2025).
[15] W. Wongniramaikul, B. Kleangklao, F. Sadegh, N. Sadegh, A. Choodum, Highly efficient phosphate adsorption using calcium silicate hydrate-embedded calcium crosslinked polyvinyl alcohol thin film, Environ. Res. 263 (3) (2024) 120229.
[16] P. Noophan, R. Rodpho, P. Sonmee, M. Hahn, S. Sirivitayaphakorn, Nutrient Remo nutrient removal performance on domestic W formance on domestic wastewater astewater treatment plants (F eatment plants (full scale system) between T ull scale system) between tropical humid opical humid and cold climates app, Environ. Res. 40 (2018) 32–39.
[17] P. Kanchanapiya, T. Tantisattayakul, Wastewater reclamation trends in Thailand, Water Sci. Technol. 86 (11) (2022) 2878–2911.
[18] S. Abdoli, S. Abdoli, B. Asgari Lajayer, Z. Dehghanian, N. Bagheri, A.H. Vafaei, M. Chamani, S. Rani, Z. Lin, W. Shu, G.W. Price, A review of the efficiency of phosphorus removal and recovery from wastewater by physicochemical and biological processes: challenges and opportunities, Water 16 (17) (2024) 2507.
[19] J.T. Bunce, E. Ndam, I.D. Ofiteru, A. Moore, D.W. Graham, A review of phosphorus removal technologies and their applicability to small-scale domestic wastewater treatment systems, front, Environ. Sci. 6 (2018) 1–15.
[20] M.N. Nadagouda, G. Varshney, V. Varshney, C.A. Hejase, Recent advances in Technologies for Phosphate Removal and Recovery: A review, ACS Environ. Au. 4 (6) (2024) 271–291.
[21] N. Abbasi, S.A. Khan, Z. Liu, T.A. Khan, Natural deep eutectic solvent (fructose-glycine) functionalized-celite/ polyethylene glycol hydrogel nanocomposite for phosphate adsorption: statistical analysis, J. Environ. Manag. 330 (2023) 117206.
[22] S. Dong, Q. Ji, Y. Wang, H. Liu, J. Qu, Enhanced phosphate removal using zirconium hydroxide encapsulated in quaternized cellulose, J. Environ. Sci. 89 (2020) 102–112.
[23] M. Hermassi, C. Valderrama, N. Moreno, O. Font, X. Querol, N. Batis, J.L. Cortina, Powdered ca-activated zeolite for phosphate removal from treated waste-water, J. Chem. Technol. Biotechnol. 91 (7) (2016) 1962–1971.
[24] J. Huo, X. Min, Y. Wang, Zirconium-modified natural clays for phosphate removal: effect of clay minerals, Environ. Res. 194 (2021) 110685.
[25] S. Kaewnoo, W. Wongniramaikul, C. Boonkanon, T. Taweekarn, B. Kleangklao, S. Limwongsakorn, C. Phawachalotorn, D.S. Aga, A. Choodum, Effective recovery of phosphate from wastewater using biodegradable calcium-rich shell wastes composite macroporous cryogel, Colloids Surf. A Physicochem. Eng. Asp. 691 (2024) 133857.
[26] C.F.Z. Lacson, M.-C. Lu, Y.-H. Huang, Calcium-based seeded precipitation for simultaneous removal of fluoride and phosphate: its optimization using BBD-RSM and defluoridation mechanism, J Water Process Eng 47 (2022) 102658.
[27] Z. Zhang, X. Wang, J. Zhao, Phosphate recovery from wastewater using calcium silicate hydrate (C-S-H): sonochemical synthesis and properties, Environ. Sci.: Water Res. Technol. 5 (1) (2019) 131–139.
[28] W. GuanX, Zhao, fluoride recovery using porous calcium silicate hydrates via spontaneous Ca2+ and OH− release, Sep. Purif. Technol. 165 (2016) 71–77.
[29] S. Ding, D. Fang, Z. Pang, B. Luo, L. Kuang, H. Wang, Q. Zhang, Q. Shen, F. Ji, Immobilization of powdery calcium silicate hydrate via PVA covalent cross-linking process for phosphorus removal, Sci. Total Environ. 645 (2018) 937–945.
[30] C. Xuechu, K. Hainan, W. Deyi, W. Xinze, L. Yongyong, Phosphate removal and recovery through crystallization of hydroxyapatite using xonotlite as seed crystal, J. Environ. Sci. 21 (5) (2009) 575–580.
[31] K. Okano, S. Miyamaru, Y. Yamamoto, M. Kunisada, H. Takano, M. Toda, K. Honda, H. Ohtake, A mobile pilot-scale plant for in situ demonstration of phosphorus recovery from wastewater using amorphous calcium silicate hydrates, Sep. Purif. Technol. 170 (2016) 116–121.
[32] K. Okano, S. Miyamaru, A. Kitao, H. Takano, T. Aketo, M. Toda, K. Honda, H. Ohtake, Amorphous calcium silicate hydrates and their possible mechanism for recovering phosphate from wastewater, Sep. Purif. Technol. 144 (2015) 63–69.
[33] E. Brakemi, K. Michael, S.P. Tan, H. Helen, Phosphate removal from wastewater using scallop and whelk shells, J Water Process Eng 55 (2023).
[34] Q. Liu, L. Guo, Y. Zhou, Y. Dai, L. Feng, J. Zhou, J. Zhao, J. Liu, G. Qian, Phosphate adsorption on biogenetic calcium carbonate minerals: effect of a crystalline phase, Desal. Water Treat. 47 (1–3) (2012) 78–85.
[35] P. Sarker, X. Liu, M.S. Rahaman, M. Maruo, Eggshell waste as a promising adsorbent for phosphorus recovery from wastewater: A review, Water Biol. Secur. 4 (1) (2025) 100319.
[36] J. Torit, D. Phihusut, Phosphorus removal from wastewater using eggshell ash, Environ. Sci. Pollut. Res. 26 (33) (2019) 34101–34109.
[37] P. Paul, S. Parbat, G. Aditya, Phosphate ion removal from aqueous solution using snail shell dust: biosorption potential of waste shells of edible snails, RSC Adv. 12 (46) (2022) 30011–30023.
[38] N.Z. Kasim, N.A.A. Abd Malek, N.S. Hairul Anuwar, N.H. Hamid, Adsorptive removal of phosphate from aqueous solution using waste chicken bone and waste cockle shell, Mater Today Proc 31 (2020) A1–A5.
[39] C. Phawachalotorn, W. Wongniramaikul, S. Kaewnoo, A. Choodum, Continuous-flow phosphate removal using cry-ca-COS monolith: insights from dynamic adsorption modeling, Water Res. X 27 (2025) 100296.
[40] C. Namasivayam, A. Sakoda, M. Suzuki, Removal of phosphate by adsorption onto oyster shell powder—kinetic studies, J. Chem. Technol. Biotechnol. 80 (3) (2005) 356–358.
[41] T.-T. Tran, N.-N.T. Tran, S. Sugiyama, J.-C. Liu, Enhanced phosphate removal by thermally pretreated waste oyster shells, J. Mater. Cycles Waste Manag. 23 (1) (2020) 177–185.
[42] J.-I. Lee, J.-K. Kang, J.-S. Oh, S.-C. Yoo, C.-G. Lee, E.-H. Jho, S.-J. Park, New insight to the use of oyster shell for removing phosphorus from aqueous solutions and fertilizing rice growth, J. Clean. Prod. 328 (2021) 129536.
[43] K. Yamashiro, R. Ikemoto, F. Ogata, S. Tanei, N. Kawasaki, Evaluation of the mechanism of phosphate removal using oyster Shell powder in aqueous environments, (in eng), Chem. Pharm. Bull. (Tokyo) 71 (8) (2023) 655–660.
[44] M. Shariati-Rad, M. Irandoust, S. Amri, M. Feyzi, F. Ja'fari, Removal, preconcentration and determination of methyl red in water samples using silica coated magnetic nanoparticles, J. Appl. Res. Water Wastewater. 1 (1) (2014) 6–12.
[45] Z. Li, Y. Sun, J. Xing, A. Meng, Fast removal of methylene blue by Fe(3)O(4) magnetic nanoparticles and their cycling property, J. Nanosci. Nanotechnol. 19 (4) (2019) 2116–2123.
[46] F. Sadegh, W. Wongniramaikul, R. Apiratikul, A. Choodum, Magnetically recyclable Fe3O4–CuS@SiO2 catalyst for synergistic adsorption and photodegradation of methyl orange in wastewater under visible light, Environ. Technol. Innov. 33 (2024) 103545.
[47] H.N. Ruslan, K. Muthusamy, S.M. Syed Mohsin, R. Jose, R. Omar, Oyster shell waste as a concrete ingredient: A review, Mater. Today Proc. 48 (2022) 713–719.
[48] L. Peng, H. Dai, Y. Wu, Z. Dai, X. Li, X. Lu, Performance and adsorption mechanism of a magnetic calcium silicate hydrate composite for phosphate removal and recovery, Water Sci. Technol. 2017 (2) (2018) 578–591.
[49] I.A. Mardiah, F.I.P. Sari, Adisyahputra, adsorption of Fe metal in groundwater by magnetite-kaolinite, IOP Conference Series: Earth Environ. Sci. 1108 (1) (2022) 012065.
[50] R. Ghelich, M.R. Jahannama, H. Abdizadeh, F.S. Torknik, M.R. Vaezi, Central composite design (CCD)-response surface methodology (RSM) of effective

electrospinning parameters on PVP-B-Hf hybrid nanofibrous composites for synthesis of HfB2-based composite nanofibers, Compos. B: Eng. 166 (2019) 527–541.
[51] S.L. Ferreira, R.E. Bruns, H.S. Ferreira, G.D. Matos, J.M. David, G.C. Brandao, E. G. da Silva, L.A. Portugal, P.S. dos Reis, A.S. Souza, W.N. dos Santos, Box-Behnken design: an alternative for the optimization of analytical methods, Anal. Chim. Acta 597 (2) (2007) 179–186.
[52] A. Choodum, B. Kleangklao, C. Boonkanon, F. Sadegh, N. Sadegh, W. Wongniramaikul, ZnCl2-doped mesoporous silica nanoparticles prepared via a simple one-pot method for highly efficient nitrate removal, Environ. Res. 267 (2025) 120711.
[53] S. Pap, C. Kirk, B. Bremner, M. Turk Sekulic, L. Shearer, S.W. Gibb, M.A. Taggart, Synthesis optimisation and characterisation of chitosan-calcite adsorbent from fishery-food waste for phosphorus removal, Environ. Sci. Pollut. Res. 27 (9) (2020) 9790–9802.
[54] Z. Yuan, Z. Xu, D. Zhang, W. Chen, T. Zhang, Y. Huang, G.L. Gu, H. Deng, D. Tian, Box-Behnken design approach towards optimization of activated carbon synthesized by co-pyrolysis of waste polyester textiles and $MgCl_2$, Appl. Surf. Sci. 427 (2018) 340–348.
[55] S. Niju, K.M. Meera, S. Begum, N. Anantharaman, Modification of egg shell and its application in biodiesel production, J. Saudi Chem. Soc. 18 (5) (2014) 702–706.
[56] J. Safaei-Ghomi, M.A. Ghasemzadeh, M. Mehrabi, Calcium oxide nanoparticles catalyzed one-step multicomponent synthesis of highly substituted pyridines in aqueous ethanol media, Scientia Iranica 20 (3) (2013) 549–554.
[57] D. Zhao, Y. Gao, Z. Liu, F. Wang, P. Liu, S. Hu, Self-assembly of honeycomb-like calcium-aluminum-silicate-hydrate (C-A-S-H) on ceramsite sand and its application in photocatalysis, Chem. Eng. J. 344 (2018) 583–593.
[58] H. Zhang, Q. Liu, J. Wang, J. Liu, H. Yan, X. Jing, B. Zhang, Preparation of magnetic calcium silicate hydrate for the efficient removal of uranium from aqueous systems, RSC Adv. 5 (8) (2015) 5904–5912, https://doi.org/10.1039/C4RA08678C.
[59] S. Kutluay, Ö. Şahin, M.Ş. Ece, Fabrication and characterization of Fe3O4/perlite, Fe3O4/perlite@SiO2, and Fe3O4/perlite@SiO2@sulfanilamide magnetic nanomaterials, Appl. Phys. A Mater. Sci. Process. 128 (3) (2022) 1–14.
[60] R. Ševčík, A. Viani, D. Machová, G. Lanzafame, L. Mancini, M.-S. Appavou, Synthetic calcium carbonate improves the effectiveness of treatments with nanolime to contrast decay in highly porous limestone, Sci. Rep. 9 (1) (2019) 15278.
[61] M.S. Djošić, V.B. Mišković-Stanković, S. Milonjić, Z.M. Kačarević-Popović, N. Bibić, J. Stojanović, Electrochemical synthesis and characterization of hydroxyapatite powders, Mater. Chem. Phys. 111 (1) (2008) 137–142.
[62] C. Phawachalotorn, W. Wongniramaikul, T. Taweekarn, B. Kleangklao, W. Pisitaro, W. Limsakul, W. Sriprom, W. Towanlong, A. Choodum, A., Continuous phosphate removal and recovery using a calcium silicate hydrate composite monolithic Cryogel column, Polymers (Basel) 15 (3) (2023) 539.
[63] D. Bi, G. Yuan, J. Wei, L. Xiao, L. Feng, Conversion of oyster Shell waste to amendment for Immobilising cadmium and arsenic in agricultural soil, Bull. Environ. Contam. Toxicol. 105 (2) (2020) 277–282.
[64] J.-H. Huh, Y.-H. Choi, C. Ramakrishna, S.H. Cheong, J.W. Ahn, Use of calcined oyster Shell powders as CO2 adsorbents in algae-containing water, J. Korean Ceram. Soc. 53 (4) (2016) 429–434.
[65] R. Maddalena, K. Li, P.A. Chater, S. Michalik, A. Hamilton, Direct synthesis of a solid calcium-silicate-hydrate (C-S-H), Constr. Build. Mater. 223 (2019) 554–565.
[66] V.A.J. Silva, P.L. Andrade, M.P.C. Silva, A. Bustamante D, L. De Los Santos Valladares, J. Albino Aguiar, Synthesis and characterization of Fe3O4 nanoparticles coated with fucan polysaccharides, J. Magn. Magn. Mater. 343 (2013) 138–143.
[67] F. Sadegh, N. Sadegh, W. Wongniramaikul, A. Choodum, Stable and magnetically separable nanocatalyst of La(OH)3-Fe3O4@rGO: an efficient solution for high-performance phosphate removal from wastewater, J Water Process Eng 70 (2025) 106923.
[68] H.-B. Kwon, C.-W. Lee, B.-S. Jun, J.-d. Yun, S.-Y. Weon, B. Koopman, Recycling waste oyster shells for eutrophication control, Resour. Conserv. Recycl. 41 (1) (2004) 75–82.
[69] H.H.T. Vu, M.D. Khan, V.T. Tran, D.V. Quang, V.A. Dao, S. Lee, J.W. Ahn, S. H. Jung, Use of calcite mud from paper factories in phosphorus treatment, Sustainability 12 (15) (2020) 5982.
[70] K.-W. Ma, H. Teng, CaO powders from oyster shells for efficient CO2 capture in multiple carbonation cycles, J. Am. Ceram. Soc. 93 (1) (2010) 221–227.
[71] D. Koizumi, K. Suzuki, H. Minamisawa, R. Togawa, K. Yasui, K. Iohara, M. Hinda, M. Aizawa, Preparation of protamine-adsorbed calcium phosphate powders and their antibacterial property, J. Asian Ceramic Soc. 10 (1) (2022) 230–240.
[72] L. Vecbiskena, K. Gross, U. Riekstina, T.C.-K. Yang, Crystallized Nano-sized alpha-Tricalcium phosphate from amorphous calcium phosphate: microstructure, cementation and cell response, Biomed. Mater. 10 (2015) 1–10.
[73] M.M. Radwan, S.M. Nagi, H.K. Abd El-Hamid, Physico-mechanical characteristics of tri-calcium silicate pastes as dentin substitute and interface analysis in class II cavities: effect of CaCl(2) and SBF solutions, Heliyon 5 (6) (2019) e01975.
[74] L. Berzina-Cimdina, N. Borodajenko, "Research of Calcium Phosphates Using Fourier Transform Infrared Spectroscopy," in *Infrared Spectroscopy - Materials Science, Engineering and Technology*, T, Theophanides ed., Rijeka, IntechOpen, 2012.
[75] A. Destainville, E. Champion, D. Bernache-Assollant, E. Laborde, Synthesis, characterization and thermal behavior of apatitic tricalcium phosphate, Mater. Chem. Phys. 80 (1) (2003) 269–277.
[76] I. García-Lodeiro, A. Fernández-Jiménez, M.T. Blanco, A. Palomo, FTIR study of the sol–gel synthesis of cementitious gels: C–S–H and N–A–S–H, J. Sol-Gel Sci. Technol. 45 (1) (2007) 63–72.
[77] S. Pap, C. Krik, B. Bremner, M.T. Sekulic, L. Shearer, S.W. Gibb, M.A. Taggart, Low-cost chitosan-calcite adsorbent development for potential phosphate removal and recovery from wastewater effluent, Water Res. 173 (2020) 115573.
[78] P. Yu, R.J. Kirkpatrick, B. Poe, P.F. McMillan, X. Cong, Structure of calcium silicate hydrate (C-S-H): near-, mid-, and far-infrared spectroscopy, J. Am. Ceram. Soc. 82 (3) (1999) 742–748.
[79] Z. Guo, K. Li, L. Jiang, Y. Ran, E.K. Sarkodie, J. Yang, J. Shi, S. Liu, M. Li, J. Li, H. Liu, Y. Liang, H. Yin, X. Liu, Removal mechanisms of phosphate from water by calcium silicate hydrate supported on hydrochar derived from microwave-assisted hydrothermal treatment, Environ. Technol. Innov. 28 (2022) 102942.
[80] B. Demri, D. Muster, XPS study of some calcium compounds, J. Mater. Process. Technol. 55 (3) (1995) 311–314.
[81] H. Chen, H. Zeng, H. Yang, Phosphate removal from wastewater by magnetic amorphous lanthanum silicate alginate hydrogel beads, Minerals 12 (2) (2022) 171.
[82] L. Black, K. Garbev, G. Beuchle, P. Stemmermann, D. Schild, X-ray photoelectron spectroscopic investigation of nanocrystalline calcium silicate hydrates synthesised by reactive milling, Cem. Concr. Res. 36 (6) (2006) 1023–1031.
[83] A. Anwar, Q. Kanwal, S. Akbar, A. Munawar, A. Durrani, M.U. Farooq, Synthesis and characterization of pure and Nanosized hydroxyapatite bioceramics, Nanotechnol. Rev. 6 (2) (2016) 149–157.
[84] V. Uskoković, X-ray photoelectron and ion scattering spectroscopic surface analyses of amorphous and crystalline calcium phosphate nanoparticles with different chemical histories, Physical Chemistry Chemical Physics 22 (10) (2020) 5531–5547, https://doi.org/10.1039/C9CP06529F.
[85] S. Pap, H. Zhang, A. Bogdan, D.T. Elsby, S.W. Gib, B. Bremmer, M.A. Taggart, Pilot-scale phosphate recovery from wastewater to create a fertiliser product: an integrated assessment of adsorbent performance and quality, Water Res. 228 (Pt B) (2023) 119369.
[86] C.C. Chusuei, D.W. Goodman, M.J. Van Stipdonk, D.R. Justes, E.A. Schweikert, Calcium phosphate phase identification using XPS and time-of-flight cluster SIMS, Anal. Chem. 71 (1) (1999) 149–153.
[87] D. Fang, L. Huang, F. Zhuoyao, Q. Zhang, Q. Shen, Y. Li, X. Xu, F. Ji, Evaluation of porous calcium silicate hydrate derived from carbide slag for removing phosphate from wastewater, Chem. Eng. J. 354 (2018) 1–11.
[88] A. Choodum, K. Mahama, P. Ramsiri, W. Wongniramaikul, Synergistic nitrate removal: enhanced efficiency with zinc-immobilized calcium cross-linked polyvinyl alcohol film, Environ. Technol. Innov. 37 (2025) 103946.
[89] K.N. Han, Characteristics of precipitation of rare earth elements with various precipitants, Minerals 10 (2) (2020) 178.
[90] P.S. Kumar, W.W. Ejerssa, C.C. Wegener, L. Korving, A.L. Dugulan, H. Temmink, M.C.M. van Loosdrecht, G.J. Witkamp, Understanding and improving the reusability of phosphate adsorbents for wastewater effluent polishing, Water Res. 145 (2018) 365–374.
[91] K. Okano, M. Uemoto, J. Kagami, K. Miura, T. Aketo, M. Toda, K. Honda, H. Ohtaka, Novel technique for phosphorus recovery from aqueous solutions using amorphous calcium silicate hydrates (A-CSHs), Water Res. 47 (7) (2013) 2251–2259.
[92] Y. Zhang, K. Yang, Y. Fang, J. Ding, H. Zhang, Removal of phosphate from wastewater with a recyclable La-based particulate adsorbent in a small-scale reactor, Water 14 (15) (2022) 2326.
[93] S.Y. Lee, J.-W. Choi, K.G. Song, K. Choi, Y.J. Lee, K.-W. Jung, Adsorption and mechanistic study for phosphate removal by rice husk-derived biochar functionalized with Mg/Al-calcined layered double hydroxides via co-pyrolysis, Compos. B Eng. 176 (2019) 107209.
[94] Y. Yao, B. Gao, M. Inyang, A.R. Zimmerman, X. Cao, P. Pullammanappallil, L. Yang, Removal of phosphate from aqueous solution by biochar derived from anaerobically digested sugar beet tailings, J. Hazard. Mater. 190 (1–3) (2011) 501–507.
[95] B.-C. Liga, B. Natalija, "Research of Calcium Phosphates Using Fourier Transform Infrared Spectroscopy," in *Infrared Spectroscopy - Materials Science, Engineering and Technology*, T, Theophanides ed., Rijeka, IntechOpen, 2012.
[96] X. Liu, F. Shen, R.L. Smith, X. Qi, Black liquor-derived calcium-activated biochar for recovery of phosphate from aqueous solutions, Bioresour. Technol. 294 (2019) 122198.
[97] D. Mitrogiannis, M. Psychoyou, I. Baziotis, V.J. Inglezakis, N. Koukouzas, N. Tsoukalas, D. Palles, E. Kamitsos, G. Oikonomou, G. Markou, Removal of phosphate from aqueous solutions by adsorption onto ca(OH)$_2$ treated natural clinoptilolite, Chem. Eng. J. 320 (2017) 510–522.
[98] B. Anes, Cristina Oliveira, R.J.N.B. da Silva, M.F. Camões, Characterization of seawaters by ion chromatography – Comparison of ionic patterns and balances, in: Presented at the IMEKO TC-19 International Workshop on Metrology for the Sea, 2019. Genoa, Italy, 3-5 October 2019.
[99] L. Li, Z. Yang, Y. Qiu, Y. Wang, Phosphorus adsorbed by HCl desorption–activated red mud adsorbents: a molecular dynamics studys, Mater Res Express 11 (4) (2024) 045507.
[100] M.N. Afridi, S. Adil, B. Byambaa, M. Sohail, A.U.R. Bacha, J. Wang, C. Li, Progress, challenges, and prospects of MOF-based adsorbents for phosphate recovery from wastewater, J Water Process Eng 63 (2024) 105530.
[101] R. Wuenscher, H. Unterfrauner, R. Peticzka, F. Zehetner, A comparison of 14 soil phosphorus extraction methods applied to 50 agricultural soils from Central Europe, plant, soil and mad, Environment 61 (2015) 86–96.

[102] N. Salim, M.A. Fulazzaky, M.H. Puteh, M.H. Khamidum, A.R.M. Yusoff, N. H. Abdullah, N. Ahmad, Z.M. Lazim, M. Nuid, Adsorption of phosphate from aqueous solutions using waste mussel shell, MATEC Web Conf. 250 (2018) 06013.
[103] Y. Feng, D. Zhao, S. Qiu, Q. He, Y. Lau, K. Zhang, S. Shen, F. Wang, Adsorption of phosphate in aqueous phase by biochar prepared from sheep manure and modified by oyster shells, ACS Omega 6 (48) (2021) 33046–33056.
[104] H. Wang, H. Luo, T. Qin, J. Yang, L. Chen, M. Liu, M. Tang, B.J. He, Z. Jing, Recyclable adsorbents of Fe and La co-modified clam shells for phosphorus removal from domestic sewage: Characterization and mechanisms, iScience 28 (2) (2025) 111762.
[105] D. Jiang, Y. Amano, M. Machida, Removal and recovery of phosphate from water by calcium-silicate composites-novel adsorbents made from waste glass and shells, Environ. Sci. Pollut. Res. Int. 24 (9) (2017) 8210–8218.
[106] Y. Kuwahara, H. Yamashita, Phosphate removal from aqueous solutions using calcium silicate hydrate prepared from blast furnace slag, ISIJ Int. 57 (9) (2017) 1657–1664.
[107] C. Li, Y. Yu, Q. Li, H. Zhong, S. Wang, Kinetics and equilibrium studies of phosphate removal from aqueous solution by calcium silicate hydrate synthesized from electrolytic manganese residue, Adsorpt. Sci. Technol. 37 (2019) 547–565, 7–8.
[108] A. Gizaw, Z. Feleke, C. Yonas, T. Melakuu, A. Mekonnen, Phosphate abatement using calcium silicate hydrate synthesized from alum factory solid waste residue, Sep. Sci. Technol. 57 (11) (2022) 1669–1687.
[109] E. Svedaite, T. Dambrauskas, A. Renman, G. Renman, K. Baltakys, Adsorption kinetics of phosphorus on a calcium silicate hydrate based adsorbent, Ceram. Int. 51 (5) (2025) 5557–5566.